This article has been accepted for inclusion in a future issue of this journal. Content is final as presented, with the exception of pagination.

Automated Adjustment of Region-Based Active Contour Parameters Using Local Image Geometry

Eleftheria A. Mylona, Michalis A. Savelonas, *Member, IEEE*, and Dimitris Maroulis, *Member, IEEE*

***Abstract*—A principled method for active contour (AC) parameterization remains a challenging issue in segmentation research, with a potential impact on the quality, objectivity, and robustness of the segmentation results. This paper introduces a novel framework for automated adjustment of region-based AC regularization and data fidelity parameters. Motivated by an isomorphism between the weighting factors of AC energy terms and the eigenvalues of structure tensors, we encode local geometry information by mining the orientation coherence in edge regions. In this light, the AC is repelled from regions of randomly oriented edges and guided toward structured edge regions. Experiments are performed on four state-of-the-art AC models, which are automatically adjusted and applied on benchmark datasets of natural, textured and biomedical images and two image restoration models. The experimental results demonstrate that the obtained segmentation quality is comparable to the one obtained by empirical parameter adjustment, without the cumbersome and time-consuming process of trial and error.**

***Index Terms*—Active contours, automated parameterization, structure tensors.**

I. Introduction

ACTIVE contours (ACs) are a rather mature image segmentation paradigm, with several variations proposed in literature [1]–[4]. However, their parameterization remains a challenging, open issue, with strong implications on the quality, objectivity, and robustness of the segmentation results. Very often, parameters are empirically adjusted on a trial and error basis, a process which is laborious and time-consuming, based on subjective as well as heuristic considerations. On one hand, nonexpert users such as medical doctors (MDs) and biologists require technical support since they are not familiar with the algorithmic inner mechanisms. On the other hand, parameter configurations of image analysis experts are usually suboptimal and applicable to specific datasets [5]. Moreover, the proliferation of AC variations raises the need for a framework facilitating fair comparisons.

Tracing the main line of progress in AC literature, one can observe that the parameterization issue persists. The first AC model, widely known as the snake model, has been proposed in the seminal work of Kass *et al*. [6]. The snake model employed physically-inspired terms for contour stiffness and rigidity, as well as image-derived terms, all weighted by empirically adjusted parameters. The snake model was succeeded by the geodesic AC model (GAC) [7]–[11] which, unlike its predecessor, is topologically adaptable and employs intrinsic contour representations instead of 1-D parameterized curves. However, GAC is still empirically parameterized. In the course of the evolution of the AC paradigm in the following years, which included edge-based [12]–[17], region-based [18]–[27] and hybrid models [28]–[33], the need for empirical parameter adjustment remained.

Numerous approaches have been proposed in order to cope with the issue of parameterization. Pluempitiwiriyawej *et al*. [34] and Tsai *et al*. [35] dynamically update AC parameters as contour evolves. This temporal dependency may lead to the propagation of early errors in the later contour evolution stages. In addition, in these approaches parameters are not spatially-varying, failing to capture local image features. Kokkinos *et al*. [36] proposed a statistical approach employing the posterior probabilities of texture, edge and intensity cues as contour weights in a locally adaptive manner. Nevertheless, their approach still requires technical skills by the domain user. Keuper *et al*. [37] and Liu *et al*. [38] presented a method for dynamic adjustment of AC parameters, applicable on the detection of cell nuclei and lip boundaries, respectively. Both methods require a priori knowledge considering the shape of the target region. Iakovidis *et al*. [39] and Hsu *et al*. [40] introduced a framework for optimization of AC parameters based on genetic algorithms. However, these heuristic approaches converge slowly in locally optimal solutions. Allili and Zhou [41] proposed an approach for estimating hyper-parameters capable of balancing the contribution of boundary and region-based terms. In their approach, empirical parameter tuning is still involved. Yushkevich *et al*. [42] developed an application for level-set segmentation of images of anatomical structures. Although their GUI is friendly to nonexpert users, parameter settings are still empirically fixed.

Manuscript received July 29, 2013; revised December 22, 2013; accepted March 28, 2014. This work was supported in part by the European Union (European Social Fund-ESF) and in part by the Greek National Funds through the Operational Program "Education and Lifelong Learning" of the National Strategic Reference Framework (NSFR)-Research Funding Program: Heracleitus II. Investing in knowledge society through the European Social Fund. This paper was recommended by Associate Editor H. Lu.

The authors are with the Realtime Systems and Image Analysis Group, Department of Informatics and Telecommunications, National and Kapodistrian University of Athens, Athens 15703, Greece (e-mail: emylona@di.uoa.gr; msavel@di.uoa.gr; dmaroulis@di.uoa.gr).

Color versions of one or more of the figures in this paper are available online at http://ieeexplore.ieee.org.

Digital Object Identifier 10.1109/TCYB.2014.2315293

This article has been accepted for inclusion in a future issue of this journal. Content is final as presented, with the exception of pagination.

This paper introduces a novel framework for automated adjustment of region-based AC regularization and data fidelity parameters based on local image geometry information. Starting from the observation that these parameters and the eigenvalues of structure tensors are associated with the same orthogonal directions, we encode local image geometry by mining the orientation coherence in edge regions. The latter can be encoded by means of orientation entropy (OE), a measure which is an increasing function of orientation variability of edges, obtaining low values in structured regions containing edges of similar orientations and high values in unstructured regions containing edges of multiple orientations. As a result, those forces that guide contour away from randomly oriented, high-entropy edge regions are amplified and iterations dedicated to erroneous local minima are avoided, speeding up contour convergence. On the other hand, forces imposed within the proximity of structured edges, naturally related to target edge regions, are reduced, enhancing segmentation accuracy. Preliminary variations of this paper have appeared in [43] and [44]. Even though these variations obtained promising segmentation results, they were only applied on a limited number of images.

It should be highlighted that the aim of this paper is to introduce a framework for automatically adjusting region-based AC parameters, rather than presenting yet another AC model. Moreover, the convergence acceleration is a byproduct of the proposed framework and not its main motivation, which is the capability of AC self-parameterization.

The contribution of the proposed framework has several aspects.

1) It is unsupervised and may be treated as a "black box": the regularization and data fidelity parameters are automatically adjusted. Hence, technical skills are not a prerequisite for the domain user and he/she is completely released from the tedious and time-consuming process of trial and error adjustment. In addition, the subjectivity of the results is reduced.
2) It is applicable to several types of images: it can be applied to natural, textured and biomedical images as well as to real-world photographs.
3) It does not require any a priori knowledge or learning considering the shape/size of the target region.
4) It guides contour away from high-entropy edge regions in order to avoid iterations dedicated to erroneous local minima, by selectively amplifying data fidelity forces.

To the best of our knowledge, this is the first paper for automated region-based AC parameterization of regularization and data fidelity energy terms combining the above elements.

The remainder of this paper is organized as follows. Section II presents the motivation behind the idea of the proposed framework, as well as its details. Section III demonstrates the results and comparisons obtained by experiments with four state-of-the-art region-based AC models and two image restoration models, which minimize an energy functional consisting of regularization and data fidelity terms. Conclusion and future research directions are summarized in Section IV.

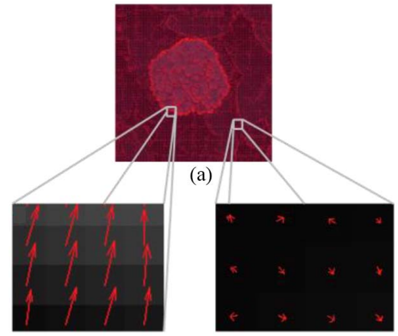

Fig. 1. (a) Structure tensor field of a test image. (b) Zoomed-in view of region which corresponds to a target edge region. (c) Zoomed-in view of region which corresponds to a nontarget edge region.

II. Proposed Framework

A. Motivation

Overviews of the standard formalisms of the most prominent AC variations can be found in [19] and [26]. The proposed framework is motivated by the attractive properties of structure tensor eigenvalues [45]. The latter are capable of describing the orientation coherence in edge regions. An edge region containing edges of similar orientations is characterized as a structured edge region, whereas an edge region containing multiple orientations is characterized as an unstructured one.

Structured edge regions correspond to target edges. This is illustrated in Fig. 1, which shows: 1) the structure tensor field of a test image; 2) a zoomed region which corresponds to a target edge region; and 3) a zoomed region which corresponds to a nontarget edge region. In the case of Fig. 1(b), the target edge region is characterized by edges of similar orientations, whereas in the case of Fig. 1(c), the nontarget edge region is associated with multiple orientations. Based on the above remark, structure tensor eigenvalues are capable of identifying whether an edge region is target or nontarget, depending on the variability of the orientations of its edges.

According to Weickert's diffusion model [46], a structure tensor D is defined as follows:

$$D = \nabla I \otimes \nabla I = \nabla I \cdot \nabla I^T \tag{1}$$

where I is an image. D has an orthonomal basis of eigenvectors v_1, v_2 with $v_1 || \nabla I$, $v_2 \perp \nabla I$ and λ_1, λ_2 are the corresponding eigenvalues defined as follows:

$$\lambda_{1,2} = \frac{1}{2}(I_{xx} + I_{yy} \pm \sqrt{(I_{xx} - I_{yy})^2 + 4I_{xy}^2} \tag{2}$$

where the + sign belongs to λ_1. The principal eigenvalue λ_1 is longitudinal with respect to the principal axis of the elliptical tensor, whereas the minor eigenvalue λ_2 is vertical with respect to the same principal axis.

Region-based ACs very often conform to Euler–Lagrange equations which consist of regularization and data fidelity terms [19]. Regularization terms are longitudinal to contour direction whereas data fidelity terms are vertical, attracting contours toward the boundaries of target edge regions. It is tempting to notice that the regularization weight, denoted as

This article has been accepted for inclusion in a future issue of this journal. Content is final as presented, with the exception of pagination.

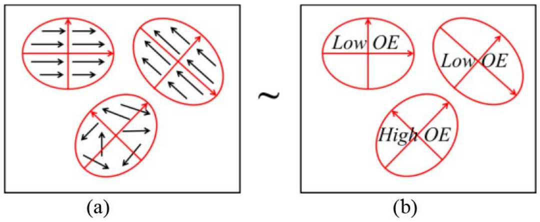

Fig. 2. Schematic representation of (a) elliptical structure tensors (red ellipses) consisting of regions of single and multiple orientations (black arrows) and (b) OE behavior on each structure tensor.

w_{reg}, corresponds to the same direction as the eigenvalue of the horizontal eigenvector of a structure tensor. Similarly, the data fidelity weight, denoted as w_{df}, corresponds to the same direction as the eigenvalue of the vertical eigenvector. This isomorphism indicates a link between the regularization and data fidelity terms and the eigenvalues of structure tensors.

B. Orientation Coherence Estimation

Motivated by the above observations, the proposed framework adjusts regularization and data fidelity parameters automatically, in a similar fashion to Weickert's diffusion model, in order to describe the orientation coherence of edge regions. The latter is calculated by orientation entropy (OE) defined as follows:

$$OE_{jk} = -\sum_{n=1}^{N_{jk}} \sum_{m=1}^{M_{jk}} p_{jk}(m,n) \cdot \log p_{jk}(m,n) \tag{3}$$

$$p_{jk} = \frac{|I_{jk}(m,n)|^2}{\sqrt{\sum_{n=1}^{N_{jk}} \sum_{m=1}^{M_{jk}} [I_{jk}(m,n)]^2}} \tag{4}$$

where I_{jk} is the subband image generated by a multidirectional filtering method such as the contourlet transform (CT) [47], OE_{jk} is the OE of the subband image I_{jk} in the k^{th} direction and the j^{th}level, M_{jk} is the row size and N_{jk} the column size of the subband image.

OE obtains high values in cases of unstructured edge regions, which are associated with noise and artifacts and low values in cases of structured edge regions, which are associated with target edges. Fig. 2(a) depicts a schematic representation of elliptical structure tensors (red ellipses) consisting of regions of single and multiple orientations (black arrows), whereas Fig. 2(b) depicts the respective OE behavior on each structure tensor.

Each $q \times q$ image grid is fed into CT through an iterative procedure. The size of the $q \times q$ image grid is experimentally determined as the minimum of the negative power of two of the original image size, which still maintains at least an edge region. For instance, in the case of the thyroid ultrasound images used in the experiments presented in Section III, it has been found that for an image of 320×320, an image grid of 40×40 ($40 = 320 \times 2^{-3}$) is suitable. The image grid is further decomposed into two pyramidal levels, which are then transformed into four directional subbands: 0°, 45°, 90°, and 135° in order to investigate whether the edge region of the grid is a target or a nontarget edge region.

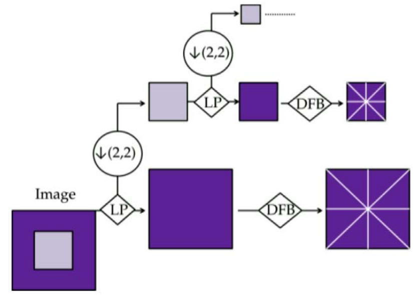

Fig. 3. CT filter-bank. LP provides a down-sampled low-pass and a band-pass version of the image. Consequently, a DFB is applied to each band-pass image.

The band-pass directional subbands represent the local image structure and apart from intensity, also hold textural information. CT provides an inherent multiscale filtering mechanism, capable of filtering out randomly oriented edges associated with noise, artifacts and/or background clutter. Moreover, CT is directly implemented in the discrete domain and is capable to selectively represent edges of various scales and directions. Small scale edges are associated with noise or artifacts.

C. Contourlet Transform (CT) [47]

Aiming at a sparse image representation, CT employs a double iterated filter-bank, which captures point discontinuities by means of the Laplacian pyramid (LP) and obtains linear structures by linking these discontinuities with a directional filter-bank (DFB). The final result is an image expansion that uses basic contour segments. Fig. 3 illustrates a CT iterated filter-bank.

The downsampled low-pass and band-pass versions of the image contain lower and higher frequencies, respectively. It is evident that, the band-pass image contains detailed information of point discontinuities, which are associated with target edge regions. Furthermore, DFB is implemented by an l-level binary tree which leads to 2^l subbands. In the first stage, a two-channel quincunx filterbank [48] with fan filters divides the 2-D spectrum into vertical and horizontal directions. In the second stage, a shearing operator reorders the samples. As a result, different directional frequencies are captured at each decomposition level. The number of iterations depends mainly on the size of the input image. The total number of directional subbands K_{total} is calculated as

$$K_{total} = \sum_{j=1}^{J} K_j \tag{5}$$

where K_j is a subband DFB applied at the j^{th} level ($j = 1, 2, ..., J$). Fig. 4 depicts the CT filter-bank of a sampled image grid, decomposed to the finest and second finest scales, which are partitioned into four directional subbands.

Among the OE values calculated for each subband, the maximum OE value of the most informative scale j and direction k, which depends on N and M is calculated and assigned to all pixels of each grid. The result is considered as an OE matrix reflecting local structure information.

This article has been accepted for inclusion in a future issue of this journal. Content is final as presented, with the exception of pagination.

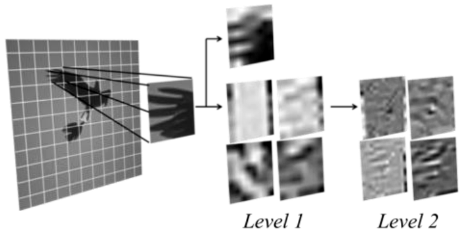

Fig. 4. CT filter-bank of a sample grid decomposed to two levels of LP and four band-pass directional subbands.

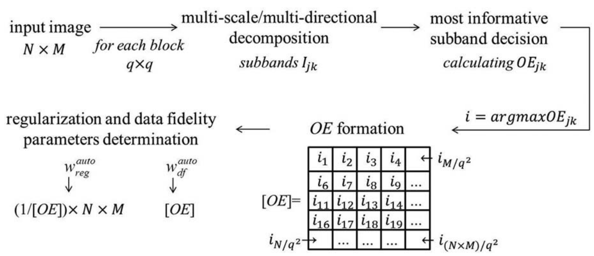

Fig. 5. Block diagram of the pipeline of the proposed framework.

D. Automated Parameterization

The regularization parameter w_{reg} and the data fidelity parameter w_{df} are matrices of the same dimensions as the original image and are calculated according to the following equations:

$$w_{reg} = (1/w_{df}) \times N \times M, \quad w_{df} = \arg_{I_{jk}} \max(OE(I_{jk})). \quad (6)$$

In cases of regions of randomly oriented edges, high values are assigned to w_{df}, amplifying data fidelity forces in the early stages of contour evolution. In such cases, contour will be repelled from the regions of randomly oriented, unstructured edges and iterations dedicated to false local minima, associated with such edges will be avoided. It should be highlighted that both parameters are calculated only once. The aim is to navigate the contour directly to structured edge regions, already from the early stages of evolution and to hinder erroneous behavior, by "constantly reminding" the locations of structured edge regions. Moreover, apart from separately adjusting each parameter, the proposed framework also achieves a balanced trade-off between regularization and data fidelity parameters. In cases of unstructured edge regions, as quantified by the maximum value of OE over all sub-band images, data provide a less reliable clue than contour regularization. On the other hand, in structured edge regions, data provide a more reliable clue. Both cases of high and low maximum OE, as well as cases with intermediate values of OE are addressed by setting regularization terms as the reciprocal of data fidelity terms.

The two spatially-varying matrices representing the automatic regularization and data fidelity parameters are integrated into the Euler–Lagrange equation, replacing the empirically determined uniform parameters. The pipeline of the proposed framework is portrayed in the block diagram of Fig. 5.

III. Results

The proposed framework has been embedded into four region-based AC models [17], [19], [26], [49] consisting of regularization and data fidelity energy terms, in order to evaluate the segmentation performance of automated versus empirical parameterization. Additionally, the proposed framework has been integrated into the Rudin–Osher–Fatima (ROF) model [50] and the Nikolova *et al.* model [51] for image restoration, so as to test its effectiveness on alternative inverse problems irrespective of the application. The well-known Chan–Vese model [19] and the model of Savelonas *et al.* [49] have been implemented in MATLAB, whilst MATLAB codes of the models of Li *et al.* [17], Bresson *et al.* [26], the ROF model [50], and the Nikolova *et al.* model [51] can be downloaded from the authors' homepages [52], [53], [54], and [55], respectively. The "9-7" biorthogonal filter for the multiscale and multidirectional decomposition stage of CT is applied [56].

The results of the original, empirically parameterized algorithms were compared to those obtained by the automated versions. Apart from the experiments on the Berkeley segmentation dataset [57] and test images obtained by various datasets [58], [59], additional experiments were conducted on 20 images of the Amsterdam library of object images (ALOI) database [60], 20 coronal scans of the lung image database consortium and image database resource initiative (LIDC-IDRI) [61], 20 thyroid ultrasound images containing hypoechoic nodules over a noisy background, provided by the radiology department of Euromedica S.A., Greece and 20 images of the labial teeth and gingiva photographic image database (LTG-IDB) [62], in order to evaluate the proposed framework on large benchmark datasets. All medical images used were investigated by MDs who provided ground truth images, whereas contour initialization was the same for both the proposed framework and the empirically fine-tuned version, in order to facilitate fair comparisons.

It should be stressed that, rather than comparing one AC method with another, the experiments to follow aim to evaluate the effectiveness of the proposed framework by examining whether the segmentation performance of the unsupervised version is at least comparable to the one obtained by the empirically fine-tuned version.

Fig. 6 illustrates: (a) and (b) test images obtained by the Berkeley dataset, (c) a thyroid ultrasound (US) test image containing a nodule, (a_1), (b_1), and (c_1) ground-truth images and (a_2), (b_2), and (c_2) segmentation results of the proposed framework. Aiming to evaluate the obtained results, the region overlap measure, known as the Tannimoto Coefficient (TC) [63], is considered

$$TC = \frac{N(A \bigcap B)}{N(A \bigcup B)} \quad (7)$$

where A is the region delineated by the segmentation method under evaluation, B is the ground truth region and $N()$ indicates the number of pixels of the enclosed region. The results of Fig. 6(a_2), (b_2), and (c_2) correspond to TC values of 90.3%, 88.7% and 91.4%, respectively.

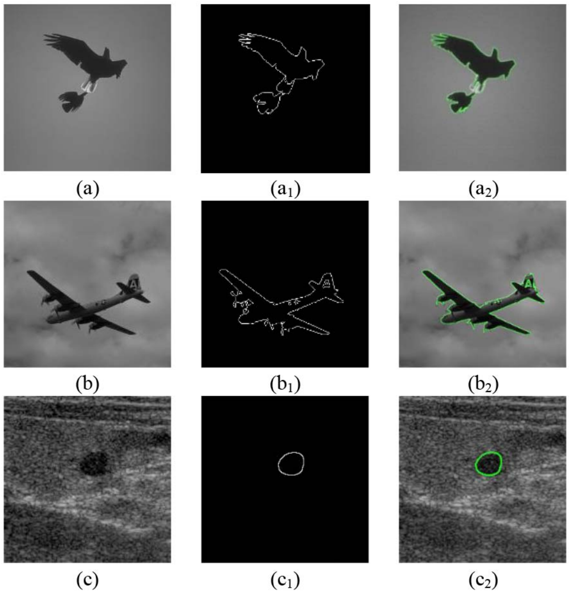

Fig. 6. Segmentation based on local image geometry. (a)–(c) Original test images. (a_1)–(c_1) Ground-truth images. (a_2)–(c_2) Segmentation results of the proposed framework.

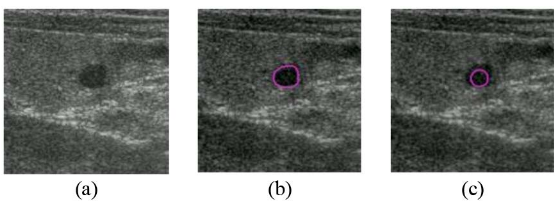

Fig. 7. (a) Sample image. (b) Segmentation results obtained by the empirically fine-tuned version ($w_{reg}^{fixed} = 0.006 \cdot 255^2$, $w_{df}^{fixed} = 1$). (c) Segmentation results obtained by the randomly-tuned version ($w_{reg}^{fixed} = 0.001 \cdot 255^2$, $w_{df}^{fixed} = 0.1$). Size 256×256.

Aiming at highlighting the significance of the proposed framework, we have investigated the sensitivity of the Chan–Vese model to small alterations of parameters. Except of being adjusted with parameters determined as optimal, the empirical version of the Chan–Vese model is also adjusted with parameters which are randomly set and is tested on sample images obtained by the utilized datasets. Accordingly, w_{reg}^{fixed} and w_{df}^{fixed} were set to randomly selected values, which fluctuated up to 10% from the optimal ones. Fig. 7 depicts: (a) a sample image, (b) segmentation results obtained by the empirically fine-tuned Chan–Vese model, and (c) segmentation results obtained by randomly tuning the same model, where w_{reg}^{fixed} and w_{df}^{fixed} were randomly set to $0.001 \cdot 255^2$ and 0.1, respectively. It is evident that, the segmentation results obtained by the random tuning differ significantly from the ones obtained by empirical fine-tuning. Random tuning leads to an average TC value of $58.3 \pm 1.7\%$, whereas empirical fine-tuning leads to an average TC value of $82.0 \pm 1.5\%$ with respect to all images tested. A similar behavior has been observed to the rest of the AC applications presented. Hence, ACs are sensitive even to small alterations of parameters and the segmentation results are highly dependent on the "optimality" of the empirical fine-tuning thus, on the technical skill of the end-user. On the contrary, the proposed framework achieves a high segmentation quality, comparable to the segmentation quality obtained by empirically fine-tuning, but in an automated fashion, endowing segmentation results with objectivity.

In the experiments to follow, evolution is stopped when the overlap between all pairs of regions enclosed by AC instances of the last five successive iterations, is more than 99.95%, as quantified by TC.

A. *Chan–Vese Model [19]*

The Chan–Vese model determines the level set evolution by solving the following equation

$$\begin{aligned}\frac{\partial \phi}{\partial t} = w_{reg}^{fixed} \cdot \delta(\phi(x, y)) \cdot div\left(\frac{\nabla \phi}{|\nabla \phi|}\right) \\ - w_{df}^{fixed}(I(x, y) - c_1)^2 + w_{df}^{fixed}(I(x, y) - c_2)^2\end{aligned} \tag{8}$$

where ϕ is the level set function, I the observed image, c_1, c_2 the average intensities inside and outside of the contour, respectively, w_{reg}^{fixed} the fixed regularization parameter and w_{df}^{fixed} the fixed data fidelity parameter. The latter are assigned the same value as suggested by Chan and Vese. For the empirical case, the optimal parameters are set according to the original paper [19]. For the proposed framework, the regularization and data fidelity parameters are automatically calculated according to (6).

The segmentation performance of the Chan–Vese model for both empirically and automatically parameterized versions is evaluated on test images obtained by [58] and [59]. The test images contain a foreground object of interest over an inhomogeneous background. The contour is initialized as a closed circle with the same center and radius for all test images and for both empirically and automatically parameterized versions, so as to ensure consistency.

Fig. 8 illustrates the contour obtained on two test images, for the second as well as for the final iteration. The first image contains an object of interest of high average intensity over a darker background, whereas the second image contains a dark object of interest over a brighter background. Yellow color is used for the initial contour in both versions whereas blue and green colors are used for the contours obtained by the empirical and automated version, on the second and final iteration.

The dilation operator has been used to morphologically reconstruct contours and enhance image appearance. In the case of the first image, the automated version converges faster to the object boundaries since the forces guiding contour evolution are appropriately amplified in nontarget, high-entropy edges. In the case of the second image, the empirical version is delayed on the fine image details and converges to erroneous boundaries. This can be explained by the gross nature of the Chan–Vese model, which is guided by region-based forces and thus, is delayed on erroneous local intensity minima associated with brighter background clutter. On the contrary, the automated version is guided by region-based forces, as well as by local geometry information, incorporated in the parameters matrices and is capable to identify the actual target edge regions.

This article has been accepted for inclusion in a future issue of this journal. Content is final as presented, with the exception of pagination.

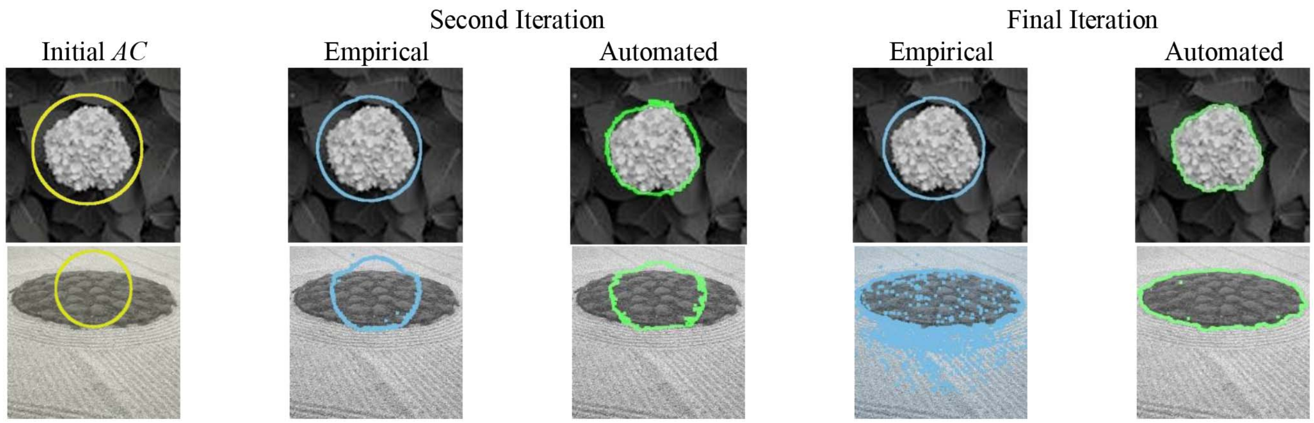

Fig. 8. Examples of contour evolution of the Chan–Vese model. Yellow color is used for the initial contour in both versions; blue and green colors are used for the contours obtained by the empirical ($w_{reg}^{fixed} = 0.006 \cdot 255^2$, $w_{df}^{fixed} = 1$) and automated version, respectively. Size 320×320.

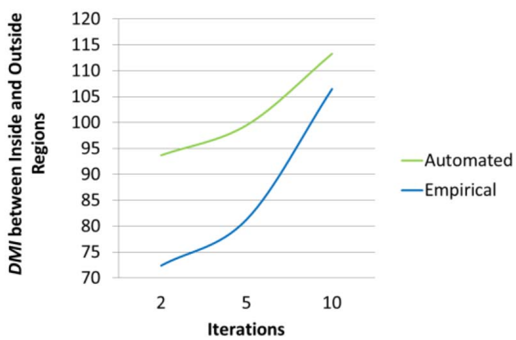

Fig. 9. DMI calculated for the early stages of evolution of the automated versus empirical version of the Chan–Vese model, presented in Fig. 8.

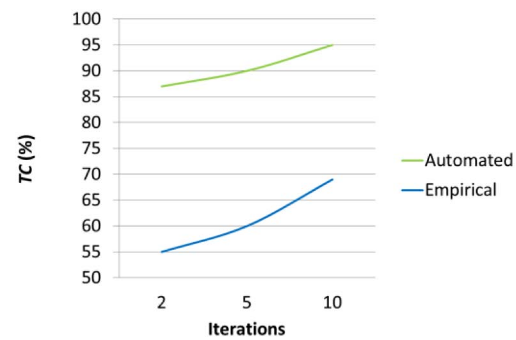

Fig. 10. TC for the early stages of evolution of automated versus empirical version presented in Fig. 8.

Aiming to evaluate the convergence rate of both versions, we define the difference of mean intensity values (DMI) between inside and outside region terms and implement the following algorithm.

$\forall$ iteration i

1. Calculate inside $|I(x, y) - c_1|^2$ and outside $|I(x, y) - c_2|^2$ region terms.
2. Normalize and quantize both terms in the range [0, 255].
3. Calculate mean values.
4. Calculate DMI.

Fig. 9 depicts DMI calculated for the early stages of evolution of the empirical and automated versions of the Chan–Vese model presented in Fig. 8. It can be observed that DMI reaches higher values in the automated case in the early stages of contour evolution. Again, this is explained by the fact that the forces guiding contour evolution are appropriately amplified in nontarget edges. Fig. 10 compares the segmentation performance of the empirical and automated version for the early stages of evolution in terms of TC.

It should be mentioned that the proposed framework is potentially applicable on similar methods which are capable of solving two-phase segmentation problems, as is the case with the model of Mory *et al*. [64].

B. Bresson et al. Model [26]

Bresson *et al*. propose to minimize the following energy functional based on the Chan–Vese model [19], in order to carry out the global minimization of segmentation

$$E(u, c_1, c_2, w_{df}^{fixed}) = TV_g(u) + w_{df}^{fixed} \int_\Omega (c_1 - I(x))^2 - (c_2 - I(x))^2 dx \quad (9)$$

where u is a characteristic function 1_{Ω_C} of a closed set where C denotes the nonconnected boundaries of Ω_C, g an edge-indicator function, $TV_g(u)$ the weighted total variation (TV) energy of the function u with the weight function g, i.e., $TV_g(u) = \int g(x)|\nabla u|dx$, and w_{df}^{fixed} the fixed data fidelity parameter. For the empirical case, the latter is set according to the original paper [26]. For the proposed framework, the data fidelity parameter is automatically calculated according to (6).

The model of Bresson *et al*. [26] is evaluated on test images obtained by the first author's homepage. Fig. 11 presents segmentation results for *Cheetah* and *Zebra* textured images. The final contour satisfies

$$\left\{(x, y) \in \Omega | I^{final}(x, y) > 0.5\right\}. \quad (10)$$

Magenta and green colors correspond to empirical and automated version, respectively. It is evident that both versions

This article has been accepted for inclusion in a future issue of this journal. Content is final as presented, with the exception of pagination.

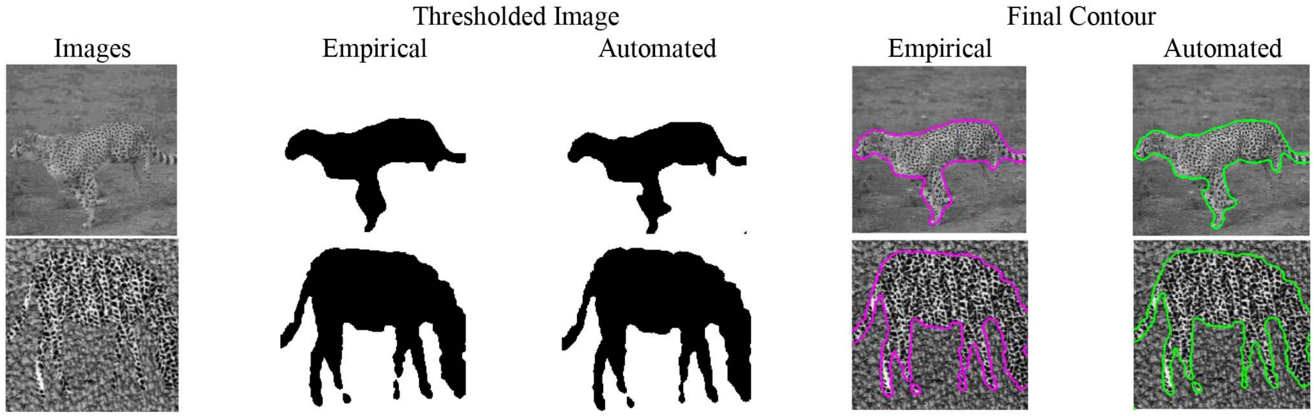

Fig. 11. Segmentation results of the model of Bresson *et al*. Magenta and green contours correspond to empirical ($w_{reg}^{fixed} = 0.7$, $w_{df}^{fixed} = 0.4$) and automated parameterization, respectively. Size 320×320.

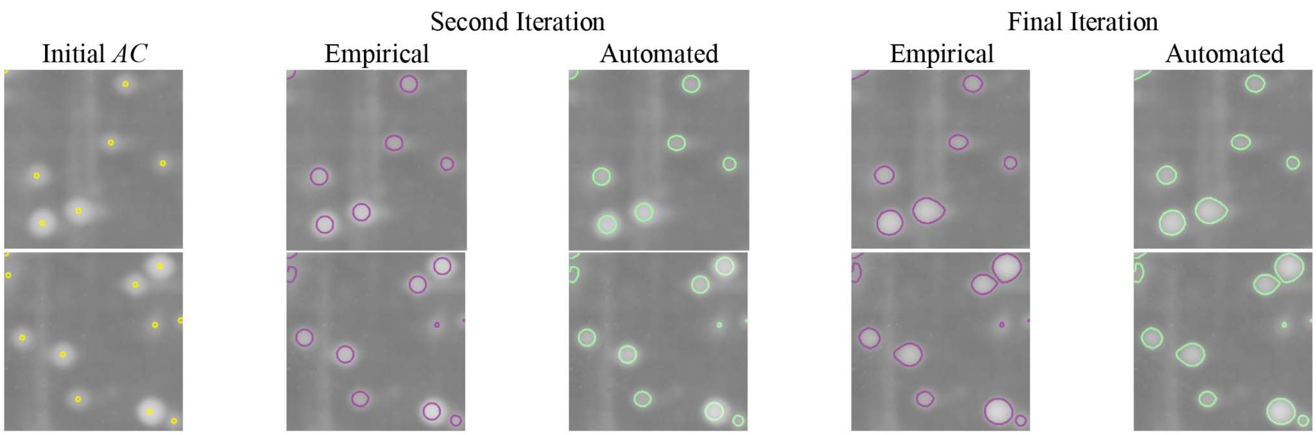

Fig. 12. Segmentation results of the model of Savelonas *et al*. Yellow is used for the initial contour in both versions, purple and green contours correspond to empirical ($w_{reg}^{fixed} = 0.006 \cdot 255^2$, $w_{df}^{fixed} = 1$) and automated parameterization, respectively. Size 320×320.

converge to the actual object boundaries, resulting in comparable segmentation accuracy. It should be pointed out that the empirical version of the model of Bresson *et al*. convexifies energy in order to compute a global minimizer. The automated version captures local geometry information correctly and converges to the actual target edge regions.

C. Savelonas et al. Model [49]

The region-based AC in Savelonas *et al*. model converges based on the Chan–Vese model [19] according to the following equation:

$$\begin{aligned}\frac{\partial\phi}{\partial t} = w_{reg}^{fixed} \cdot \delta(\phi(x,y)) \cdot div\left(\frac{\nabla\phi}{|\nabla\phi|}\right) \\ -w_{df_1}^{fixed}(I_1(x,y)-c_1)^2 + w_{df_1}^{fixed}(I_1(x,y)-c_2)^2 \\ -w_{df_2}^{fixed}(I_2(x,y)-c_3)^2 + w_{df_2}^{fixed}(I_2(x,y)-c_4)^2\end{aligned} \quad (11)$$

where ϕ is the level set function, I_1, I_2 the observed image and the binarized image which is the output of morphological processing, respectively, c_1, c_2 and c_3, c_4 the average intensities inside and outside of the contour of I_1 and I_2, respectively, w_{reg}^{fixed} the fixed regularization parameter, $w_{df_1}^{fixed}$ and $w_{df_2}^{fixed}$ the fixed data fidelity parameters of I_1 and I_2, respectively. For the empirical case, the optimal parameters are set according to the original paper [49]. For the proposed framework, the regularization and data fidelity parameters are automatically calculated according to (6). The segmentation performance of the recent model of Savelonas *et al*. for both empirical and automated versions is evaluated on real 2-D gel electrophoresis (2D-GE) images, obtained by the Biomedical Research Foundation of the Academy of Athens.

Fig. 12 illustrates contours obtained on the second as well as on the final iteration, for 2D-GE sub-images. Yellow color is used for the initial contour in both versions, whereas purple and green colors correspond to empirical and automated version, respectively. It is evident that the segmentation results of the empirical and automated versions are comparable. Nonetheless, as already pointed out, empirical parameterization requires tedious, time-consuming experimentation. Our framework is capable of obtaining comparable results in an automated fashion. Fig. 13 depicts DMI for both versions, for the early stages of contour evolution presented in Fig. 12. Again in the case of the automated version, DMI is slightly higher in early iterations.

In Fig. 14, the comparison is performed in terms of TC, providing a quantification of the actual segmentation performance for the early stages of evolution. So far, the proposed framework has been applied on region-based AC models.

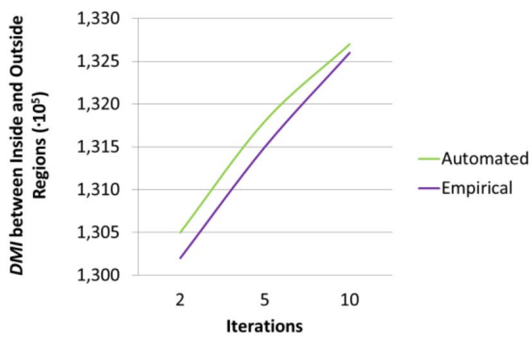

Fig. 13. DMI between inside and outside regions for the early stages of evolution of automated versus empirical version presented in Fig. 12.

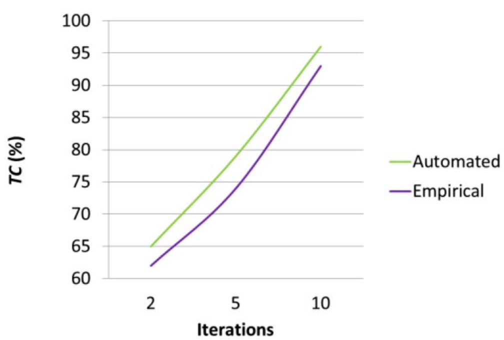

Fig. 14. TC for the early stages of evolution of automated versus empirical version presented in Fig. 12.

D. Li et al. Model [17]

The proposed framework has also been applied on the model of Li *et al*. so as to investigate its effectiveness on AC models which are not purely region-based, with respect to data fidelity and regularization parameters. In this sense, the two parameters automatically fine-tuned were w_{df}^{fixed} and w_{reg}^{fixed}, since these two parameters correspond to data fidelity and regularization parameters, for which the proposed framework has been formulated. Li *et al*. minimize an energy functional inspired by the GAC energy functional [10], which is defined as

$$E(\phi) = w_{reg}^{fixed} \int_{\Omega} p(|\nabla\phi|dx + a^{fixed} \int_{\Omega} g\delta_{\varepsilon}(\phi)|\nabla\phi|dx + w_{df}^{fixed} \int_{\Omega} gH_{\varepsilon}(-\phi)dx \quad (12)$$

where ϕ is the level set function, p a potential function p:$[0, \infty) \to \Re$, g an edge-indicator function, δ the Dirac function, H the Heaviside function, w_{reg}^{fixed} the fixed regularization parameter, a^{fixed} a fixed parameter that weights the second energy term which can be expressed as a line integral of the GAC model, and w_{df}^{fixed} the fixed data fidelity parameter. The level set evolution is determined as follows:

$$\frac{\partial\phi}{\partial t} = w_{reg}^{fixed} \cdot div\left(d_p \frac{\nabla\phi}{|\nabla\phi|}\right) + a^{fixed}\delta_{\varepsilon}(\phi) \cdot div\left(g\frac{\nabla\phi}{|\nabla\phi|}\right) + w_{df}^{fixed} g\delta_{\varepsilon}(\phi). \quad (13)$$

For the empirical case, the optimal fixed parameters are set according to the original paper [17]. For the proposed framework, the optimal fixed value of a^{fixed} is maintained, whereas the regularization and data fidelity parameters are automatically calculated according to (6). The value of a^{fixed} remained empirically fixed and its adjustment is beyond the scope of this paper. However, the presence of the extra term in this model did not prevent the proposed framework to automatically adjust w_{reg}^{fixed} and w_{df}^{fixed}.

In a similar fashion, the segmentation performance of both empirical and automated versions of the model of Li *et al*. [17] is evaluated on test images obtained by the author's homepage [52]. Fig. 15(a) and (b) illustrates a test image and the initial level-set function, respectively, whereas the images below present contours obtained in three different iterations, as well as the final level-set functions. The latter exhibit the shape of a signed distance function in the vicinity of the zero level-set and a flat shape outside this vicinity. Red and green colors correspond to empirical and automated parameterization, respectively. It should be pointed out that the level-set evolution is applied without reinitialization and is guided also by edge-based forces. It is evident that the segmentation results of the empirical and automated versions are comparable.

Fig. 16 depicts TC results of both empirical and automated versions for the early stages of contour evolution presented in Fig. 15. In the automated version, TC reaches slightly higher values from early iterations. However, one should take into account that with empirical parameterization it is always possible to set "optimal" parameters after laborious, time-consuming experimentation. Our framework is capable of obtaining comparable results in an automated fashion.

E. Rudin–Osher–Fatima (ROF) Model [50]

The proposed framework is also integrated into the ROF model for edge-preserving image restoration, so as to test its effectiveness on other inverse minimization problems (TV minimization). The aim of the ROF model is to remove noise from a corrupted image without blurring the target edges. Let $f = K * I + n$ denote the image plagued by noise, where K, n are the convolution kernel and additive noise, respectively. The "clean" image is recovered by minimizing the following energy:

$$E(I) = \int_{\Omega} |\nabla I| + w_{df}^{fixed} \int_{\Omega} (f - I)^2 dx. \quad (14)$$

For the empirical case, the optimal fixed parameter is set according to the original paper [50]. For the proposed framework, the data fidelity parameter is automatically calculated according to (6). Fig. 17 illustrates: (a) the original image plagued by noise, (b) the recovered image of the ROF model utilizing empirical parameterization, and (c) the recovered image of the ROF model utilizing automated parameterization. In [50], image restoration is visually assessed. Following this, it can be observed that, the automated version maintains the quality of image restoration, originally obtained with empirical parameters.

F. Nikolova et al. Model [51]

The Nikolova *et al*. model solve the following nonconvex nonsmooth minimization problem for image restoration and reconstruction:

$$J(I, u) = ||HI - g||_2^2 + \beta\Psi(I) + \beta\alpha TV(u) + w_{df}^{fixed}||I - u||_2^2 \quad (15)$$

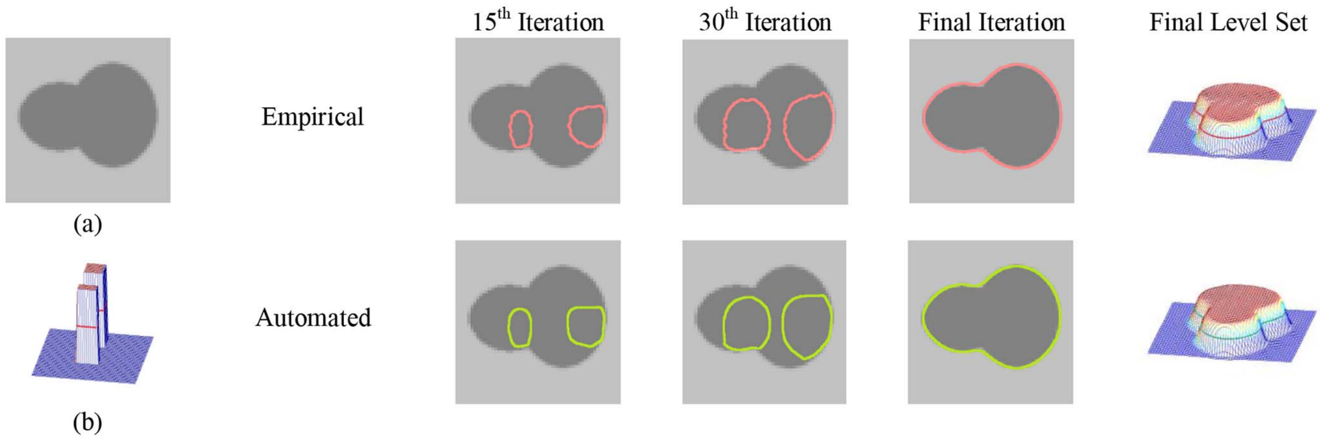

Fig. 15. Evolution of segmentation for the model of Li *et al*. Red and green contour corresponds to empirical ($w_{reg}^{fixed} = 0.2$, $w_{df}^{fixed} = 5$) and automated parameterization, respectively. (a) Original test image. (b) Initial level-set function. Size 56×56.

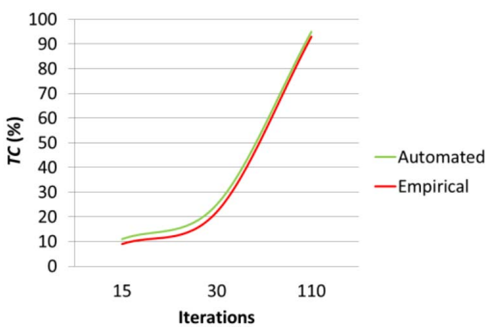

Fig. 16. TC for the early stages of evolution of automated versus empirical model presented in Fig. 15.

where H is a $q \times p$ matrix representing optical blurring, $\Psi(\mathrm{I}) = \sum_{i \in I} \psi_\varepsilon(||D_i I||_2$, where ψ is a smooth and concave function and D_i discrete gradients, g the image plagued by noise, $u \in \Re$ an auxiliary variable used to transfer the nonsmooth TV term from image I and β, α the restoration parameters, where β is a regularization parameter and α a positive parameter. In the case of empirical fine-tuning, the fixed parameter w_{df}^{fixed} is set according to the original paper [51]. In the case of the proposed framework, the data fidelity parameter is automatically calculated according to (6). Fig. 18 illustrates: (a) the original image, (b) the observed image, (c) the result of empirically parameterized restoration, and (d) the result of restoration parameterized by means of (6). It is once more evident that, the proposed framework maintains the quality of image restoration compared to the one obtained by empirical parameterization. In more quantitative terms, the point-to-signal-noise-ratio (PSNR) obtained by empirical and automated parameterization is 18.65 and 18.59 dB, respectively.

Considering both the ROF model and the Nikolova *et al*. model, it should be highlighted that, even though the proposed framework has been designed for segmentation models, it can also be effectively embedded in other energy minimization models, with similar formulation, as is the case of these two restoration models.

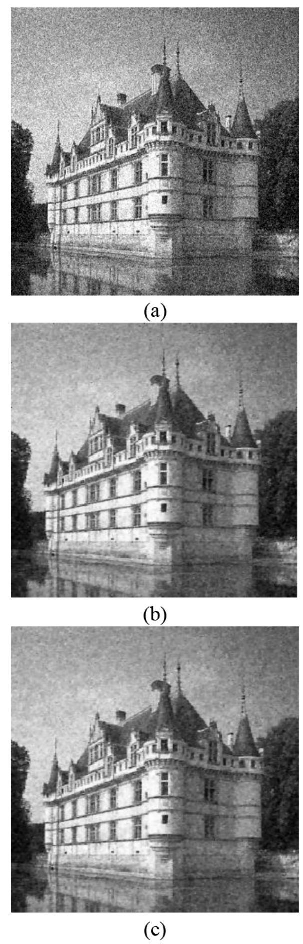

Fig. 17. (a) Original image plagued by noise, the recovered image of the ROF model utilizing. (b) Empirical parameterization ($w_{df}^{fixed} = 12$). (c) Automated parameterization. Size 320×320.

G. Additional Experiments on Various Datasets

The proposed framework is also tested on 20 grayscale images obtained by the ALOI database [60], 20 coronal scans obtained by the LIDC-IDRI [61], 20 thyroid ultrasound

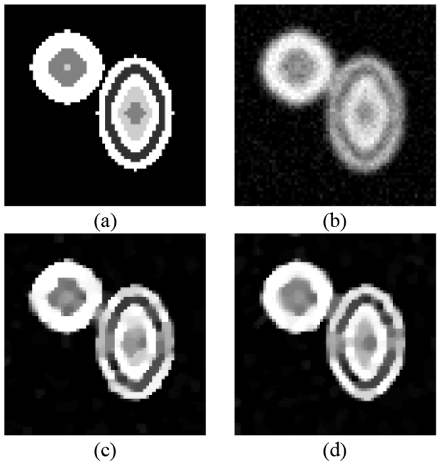

Fig. 18. (a) Original image plagued by noise. (b) Observed image. (c) Restored image utilizing empirical parameterization ($w_{df}^{fixed} = 0.05$). (d) Restored image utilizing automated parameterization. Size 64×64.

images containing hypoechoic nodules provided by the radiology department of Euromedica S.A., Greece and 20 images obtained by the LTG-IDB [62] in order to enable evaluation on large benchmark datasets.

Fig. 19 illustrates segmentation results on sample images obtained by the ALOI database for both empirical and automated parameterization. The first and second columns illustrate test images and their ground truth, respectively. The third column provides the iteration number, for which the automated version converges. The fourth and fifth columns illustrate segmentation results of the empirical and automated case for that iteration, respectively. The sixth and seventh columns illustrate the iteration number for which the empirical version converges and the segmentation results for that iteration, respectively. All test images were recorded with varying viewing and illumination angles, resulting in challenging shades. Several images of ALOI database, including the illustrated *Teapot*, *Bear*, *Basket*, and *Wire*, contain intensity-based information whereas some also contain textured regions, as is the case with *Basket* and *Wire*. It is evident that after convergence, the segmentation results of both empirical and automated versions are comparable. However, in the empirical case, the contour is delayed on erroneous local intensity minima associated with shades and thus requires approximately 10–20 times more iterations in order to converge. On the contrary, in the automated case, forces which guide contour evolution are appropriately amplified in nontarget, high-entropy edges, accelerating convergence. The automated case achieves an average TC value of 96.9 ± 1.6%, which is comparable to the TC value obtained by the empirical case. However, the empirical case achieves a TC value of 58.4 ± 14.3% in the same iteration that the automated version has converged, with regards to all ALOI images tested.

Fig. 20 illustrates: (a)–(c) sample coronal computed-tomography scans of lung parenchyma, (a_1)–(c_1) ground truth images, (a_2)–(c_2) segmentation results of the empirical version, (a_3)–(c_3) segmentation results of the automated version. The aim of segmentation on this database (LIDC-IDRI) is to separate the lung parenchyma from the surrounding anatomy, which is typically impeded by airways or other "airway-like" structures in the right and left lung. The segmentation result is used for the computation of emphysema measures. Such images contain an inhomogeneous background and multiple features, such as the trachea and thoracic spine (pale areas), as well as the left and right lung (dark areas). It is notable that both versions achieve comparable segmentation results. The automated version achieves an average TC value of 83.8 ± 1.3%, over all computed-tomography scans of the database, which is comparable to the TC value of 82.5 ± 1.8% obtained by the empirical version.

Fig. 21 illustrates: (a)–(c) sample thyroid ultrasound images containing hypoechoic nodules, (a_1)–(c_1) ground truth images, (a_2)–(c_2) segmentation results of the empirical version, (a_3)–(c_3) segmentation results of the automated version. Hypoechoic nodules may be associated with medium or high risk for malignancy, depending on the irregularity of their boundary. These images are very challenging with respect to segmentation, since they are plagued by speckle noise and artifacts. Moreover, thyroid nodules are characterized by blurred and irregular boundaries. It can be observed that the segmentation result of the automated version is comparable to the one obtained by the empirical version. The automated version achieves an average TC value of 83.7 ± 0.8%, over all thyroid ultrasound images of the database, which is comparable to the TC value of 82.8 ± 1.2% obtained by the empirical version.

Fig. 22 illustrates: (a)–(c) labial teeth and gingiva photographic images, (a_1)–(c_1) ground truth images, (a_2)–(c_2) segmentation results of the empirical version, (a_3)–(c_3) segmentation results of the automated version. The scope of this database (LTG-IDB) is the task of teeth/nonteeth segmentation. Such images are characterized by intensity variations from saturated to faint areas, over an inhomogeneous background (gingiva). It can be observed that the segmentation results obtained by the automated version approximate the corresponding ground truth images. The automated version achieves an average TC value of 84.2 ± 1.8%, over all images of the database, which is comparable to the TC value of 82.9 ± 1.6% obtained by the empirical version.

IV. Conclusion and Future Directions

This paper introduces a novel framework for automated regularization and data fidelity parameterization of region-based ACs, which is motivated by the observation that the weighting factors of regularization and data fidelity terms and the eigenvalues of structure tensors are associated with the same orthogonal directions. The proposed framework is unsupervised and does not require technical skills from the domain user. In addition, it is applicable to several image modalities and does not require prior knowledge on the target regions. Moreover, it avoids iterations dedicated to erroneous local minima, resulting in convergence rate comparable to or higher than the one obtained with empirical parameterization.

The proposed framework has been experimentally evaluated on various datasets of natural, textured, and biomedical images

This article has been accepted for inclusion in a future issue of this journal. Content is final as presented, with the exception of pagination.

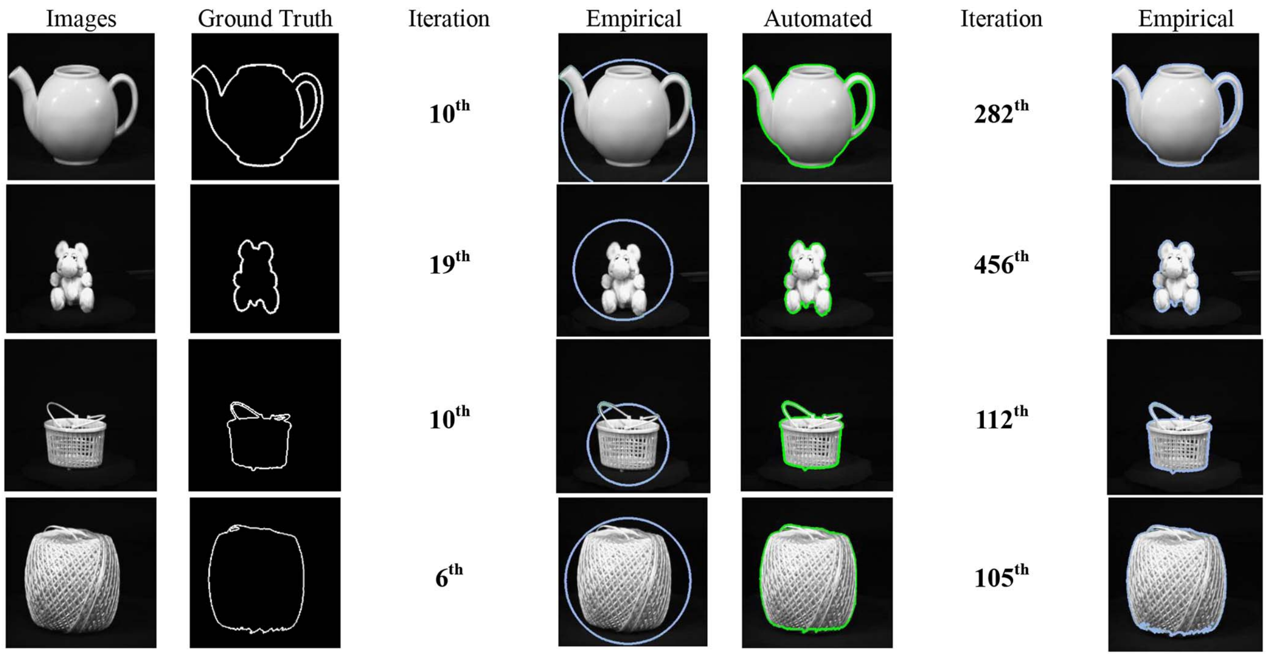

Fig. 19. Segmentation results of the proposed framework. The first and second columns illustrate test images obtained by ALOI database [60] and their ground truth images, respectively. The third column shows the final iteration of contour convergence in the automated case. The fourth and fifth column illustrates segmentation results of the empirical ($w_{reg}^{fixed} = 0.006 \cdot 255^2$, $w_{df}^{fixed} = 1$) and automated case for that iteration, respectively. The sixth and seventh column illustrates the final iteration of contour convergence in the empirical case as well as the segmentation results for that iteration, respectively. Size 320×320.

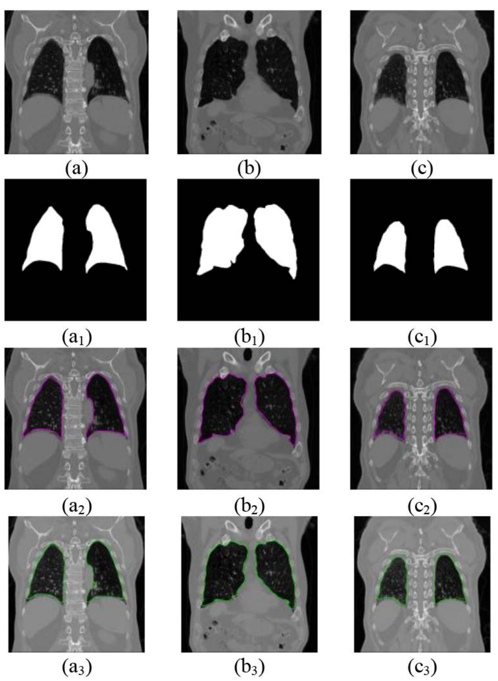

Fig. 20. (a)–(c) Coronal computed-tomography scans of lung parenchyma. (a_1)–(c_1) Ground truth images. (a_2)–(c_2) Segmentation results of the empirical version ($w_{reg}^{fixed} = 0.006 \cdot 255^2$, $w_{df}^{fixed} = 1$). (a_3)–(c_3) Segmentation results of the automated version. Size 320×320.

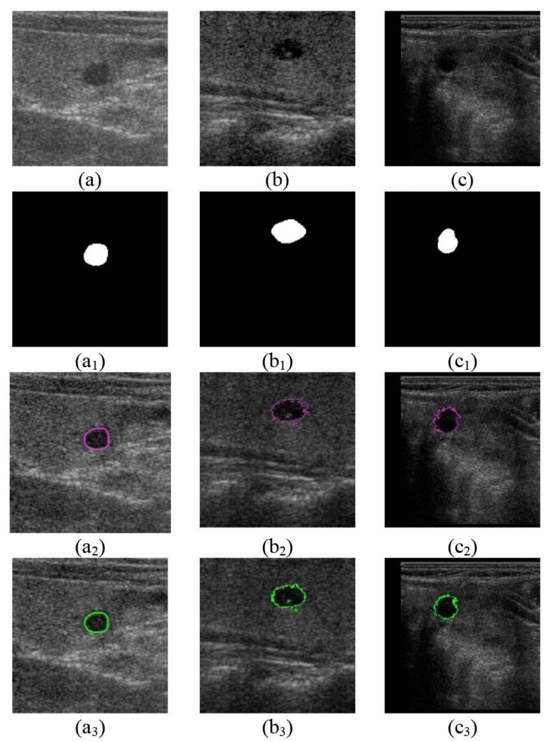

Fig. 21. (a)–(c) Thyroid ultrasound images containing nodules. (a_1)–(c_1) Ground truth images. (a_2)–(c_2) segmentation results of the empirical version ($w_{reg}^{fixed} = 0.006 \cdot 255^2$, $w_{df}^{fixed} = 1$). (a_3)–(c_3) Segmentation results of the automated version. Size 256×256.

by comparing the segmentation performance obtained by empirical versus automated parameterization of four state-of-the-art region-based AC variations and two image restoration models. The experimental results show that it is capable of maintaining a segmentation quality comparable to the one obtained with empirical parameterization, yet in an automated fashion. Future directions of this paper include investigation

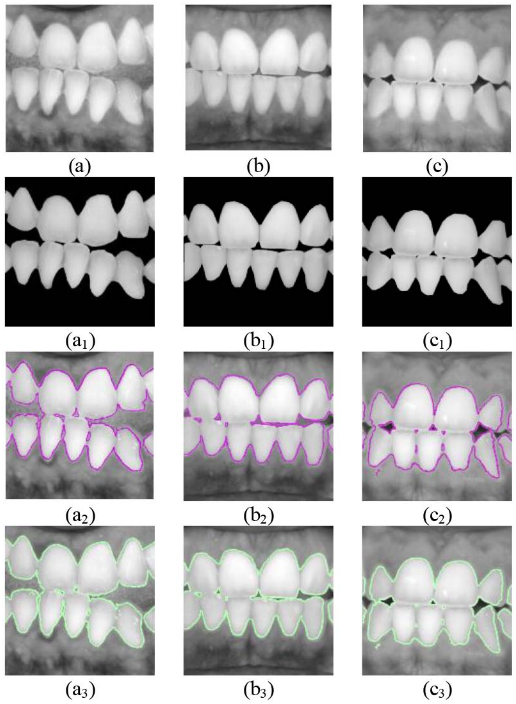

Fig. 22. (a)–(c) Labial teeth and gingiva photographic images. (a_1)–(c_1) Ground truth images. (a_2)–(c_2) Segmentation results of the empirical version ($w_{reg}^{fixed} = 0.006 \cdot 255^2$, $w_{df}^{fixed} = 1$). (a_3)–(c_3) Segmentation results of the automated version. Size 320×320.

of the potential of alternative instances of the proposed framework on several biomedical application domains.

Acknowledgment

The authors would like to thank Prof. R. Deriche for his fruitful comments during his visit to the Department of Informatics and Telecommunications of the National and Kapodistrian University of Athens. They would also like to thank the Biomedical Research Foundation of the Academy of Athens for the provision of real 2D-GE images, and Dr. N. Dimitropoulos, MD Radiologist, EUROMEDICA S.A., Greece, for providing the thyroid ultrasound images. They are grateful to the reviewers for their constructive comments and suggestions.

References

[1] Y. Rathi, N. Vaswani, A. Tannenbaum, and A. Yezzi, "Tracking deformable objects using particle filtering for geometric active contours," *IEEE Trans. Pattern Anal. Mach. Intell.*, vol. 29, no. 8, pp. 1470–1475, Aug. 2007.

[2] G. Sundaramoorthi, A. Yezzi, and A. Mennucci, "Coarse-to-fine segmentation and tracking using Sobolev active contours," *IEEE Trans. Pattern Anal. Mach. Intell.*, vol. 30, no. 5, pp. 851–864, May 2008.

[3] A. Mishra, P. W. Fieguth, and D. A. Clausi, "From active contours to active surfaces," in *Proc. IEEE CVPR*, Providence, RI, USA, 2011, pp. 2121–2128.

[4] V. Appia and A. Yezzi, "Active geodesics: Region-based active contour segmentation with a global edge-based constraint," in *Proc. IEEE ICCV*, Barcelona, Spain, 2011, pp. 1975–1980.

[5] H. Xiao, Y. Li, J. Du, and A. Mosig, "Ct3d: Tracking microglia motility in 3D using a novel cosegmentation approach," *Bioinformatics*, vol. 28, no. 4, pp. 564–571, 2011.

[6] M. Kass, A. Witkin, and D. Terzopoulos, "Snakes: Active contour models," *Int. J. Comput. Vis.*, vol. 1, no. 4, pp. 321–331, 1988.

[7] V. Caselles, R. Kimmel, and G. Sapiro, "Geodesic active contours," in *Proc. IEEE ICCV*, Cambridge, MA, USA, 1995, pp. 694–699.

[8] S. Kichenassamy, A. Kumar, P. Olver, A. Tannenbaum, and A. Yezzi, "Gradient flows and geometric active contour models," in *Proc. IEEE ICCV*, Cambridge, MA, USA, 1995, pp. 810–815.

[9] R. Malladi, J. A. Sethian, and B. C. Vemuri, "Shape modeling with front propagation: A level set approach," *IEEE Trans. Pattern Anal. Mach. Intell.*, vol. 17, no. 2, pp. 158–175, Feb. 1995.

[10] N. Paragios and R. Deriche, "Geodesic active contours and level sets for the detection and tracking of moving objects," *IEEE Trans. Pattern Anal. Mach. Intell.*, vol. 22, no. 3, pp. 266–280, Mar. 2000.

[11] S. Osher and J. Sethian, "Fronts propagating with curvature-dependent speed: Algorithms based on the Hamilton–Jacobi formulation," *J. Comput. Phys.*, vol. 79, no. 1, pp. 12–49, 1988.

[12] M. Leventon, W. Grimson, and O. Faugeras, "Statistical shape influence in geodesic active contours," in *Proc. IEEE Conf. CVPR*, vol. 1. Hilton Head Island, SC, USA, 2000, pp. 316–323.

[13] J. Daugman, "New methods in iris recognition," *IEEE Trans. Syst., Man, Cybern. B, Cybern.*, vol. 37, no. 5, pp. 1167–1175, Oct. 2007.

[14] N. Paragios, O. Mellina-Gottardo, and V. Ramesh, "Gradient vector flow fast geometric active contours," *IEEE Trans. Pattern Anal. Mach. Intell.*, vol. 26, no. 3, pp. 402–407, Mar. 2004.

[15] C. Li, C. Xu, C. Gui, and M. D. Fox, "Level set evolution without reinitialization: A new variational formulation," in *Proc. IEEE Conf. CVPR*, vol. 1. 2005, pp. 430–436.

[16] X. Xie and M. Mirmehdi, "MAC: Magnetostatic active contour model," *IEEE Trans. Pattern Anal. Mach. Intell.*, vol. 30, no. 4, pp. 632–646, Apr. 2008.

[17] C. Li, C. Xu, C. Gui, and M. D. Fox, "Distance regularized level set evolution and its application to image segmentation," *IEEE Trans. Image Process.*, vol. 19, no. 12, pp. 3243–3254, Dec. 2010.

[18] D. Mumford and J. Shah, "Boundary detection by minimizing functionals," in *Proc. IEEE Conf. CVPR*, 1985, pp. 22–26.

[19] T. F. Chan and L. A. Vese, "Active contours without edges," *IEEE Trans. Image Process.*, vol. 10, no. 2, pp. 266–277, Feb. 2001.

[20] A. Tsai, A. Yezzi, and A. S. Willsky, "Curve evolution implementation of the Mumford–Shah functional for image segmentation, denoising, interpolation and magnification," *IEEE Trans. Image Process.*, vol. 10, no. 8, pp. 1169–1186, Aug. 2001.

[21] L. A. Vese and T. F. Chan, "A multiphase level set framework for image segmentation using the Mumford and Shah model," *Int. J. Comput. Vis.*, vol. 50, no. 3, pp. 271–293, 2002.

[22] D. Freedman and T. Zhang, "Active contours for tracking distributions," *IEEE Trans. Image Process.*, vol. 13, no. 4, pp. 518–526, Apr. 2004.

[23] P. Li, "Tensor-SIFT based earth mover's distance for contour tracking," *J. Math. Imaging Vis.,* vol. 46, no. 1, pp. 44–65, 2013.

[24] S. Jehan-Besson, M. Barlaud, G. Aubert, and O. Faugeras, "Shape gradients for histogram segmentation using active contours," in *Proc. IEEE ICCV*, Nice, France, 2003, pp. 408–415.

[25] T. Brox and D. Cremers, "On local region models and a statistical interpretation of the piecewise smooth Mumford-Shah functional," *Int. J. Comput. Vis.*, vol. 84, no. 2, pp. 184–193, Aug. 2009.

[26] X. Bresson, S. Esedoglu, P. Vandergheynst, J. Thiran, and S. Osher, "Fast global minimization of the active contour/snake model," *J. Math. Imaging Vis.*, vol. 28, no. 2, pp. 151–167, 2007.

[27] E. Strekalovskiy, A. Chambolle, and D. Cremers, "A convex representation for the vectorial Mumford-Shah functional," in *Proc. IEEE Conf. CVPR*, Providence, RI, USA, 2012.

[28] N. Paragios and R. Deriche, "Geodesic active regions and level set methods for supervised texture segmentation," *Int. J. Comput. Vis.*, vol. 46, no. 3, pp. 223–247, 2002.

[29] C. Li, C. Kao, J. Gore, and Z. Ding, "Implicit active contours driven by local binary fitting energy," in *Proc. IEEE Conf. CVPR*, Minneapolis, MN, USA, 2007, pp. 1–7.

[30] S. Lankton and A. Tannenbaum, "Localizing region-based active contours," *IEEE Trans. Image Process.*, vol. 17, no. 11, pp. 2029–2039, Nov. 2008.

[31] R. S. T. Lee and J. N. K. Lin, "An elastic contour matching model for tropical cyclone pattern recognition," *IEEE Trans. Syst., Man, Cybern. B, Cybern.*, vol. 31, no. 3, pp. 413–417, Jun. 2001.

[32] L. Wang, C. Li, Q. Sun, D. Xia, and C. Kao, "Active contours driven by local and global intensity fitting energy with application to brain MR image segmentation," *Comput. Med. Imaging Graph.*, vol. 33, no. 7, pp. 520–531, 2009.

[33] B. Wu and Y. Yang, "Local- and global-statistics-based active contour model for image segmentation," *Math. Probl. Eng.*, vol. 64, Article 791958, Jan. 2012.

[34] C. Pluempitiwiriyawej, J. M. F. Moura, Y. J. L. Wu, and C. Ho, "STACS: New active contour scheme for cardiac MR image segmentation," *IEEE Trans. Med. Imag.*, vol. 24, no. 5, pp. 593–603, May 2005.
[35] A. Tsai *et al.*, "A shape-based approach to the segmentation of medical imagery using level sets," *IEEE Trans. Med. Imag.*, vol. 22, no. 2, pp. 137–154, Feb. 2003.
[36] I. Kokkinos, G. Evangelopoulos, and P. Maragos, "Texture analysis and segmentation using modulation features, generative models and weighted curve evolution," *IEEE Trans. Pattern Anal. Mach. Intell.*, vol. 31, no. 1, pp. 142–157, Jan. 2009.
[37] M. Keuper *et al.*, "3D deformable surfaces with locally self-adjusting parameters—A robust method to determine cell nucleus shapes," in *Proc. IEEE ICPR*, Washington, DC, USA, 2010, pp. 2254–2257.
[38] X. Liu, Y. M. Cheung, M. Li, and H. Liu, "A lip extraction method using localized active contour model with automatic parameter selection," in *Proc. IEEE ICPR*, Istanbul, Turkey, 2010, pp. 4332–4335.
[39] D. Iakovidis, M. Savelonas, S. Karkanis, and D. Maroulis, "A genetically optimized level set approach to segmentation of thyroid ultrasound images," *Appl. Intell.*, vol. 27, no. 3, pp. 193–203, Dec. 2007.
[40] C. Y. Hsu, C. Y. Liu, and C. M. Chen, "Automatic segmentation of liver PET images," *Comput. Med. Imaging Graph.*, vol. 32, no. 7, pp. 601–610, 2008.
[41] M. Allili and D. Ziou, "An approach for dynamic combination of region and boundary information in segmentation," in *Proc. IEEE ICPR*, Tampa, FL, USA, 2008, pp. 1–4.
[42] P. A. Yushkevich *et al.*, "User-guided level set segmentation of anatomical structures with ITK–SNAP," in *Proc. Insight J., Special Issue ISC/NA-MIC/MICCAI Workshop Open-Source Software*, 2005.
[43] E. A. Mylona, M. A. Savelonas, and D. Maroulis, "Entropy-based spatially-varying adjustment of active contour parameters," in *Proc. IEEE ICIP*, Orlando, FL, USA, 2012, pp. 2565–2568.
[44] E. A. Mylona, M. A. Savelonas, D. Maroulis, and A. N. Skodras, "Autopilot spatially-adaptive active contour parameterization for medical image segmentation," in *Proc. IEEE Int. Symp. CBMS*, Porto, Portugal, 2013.
[45] D. Tschumperlé and R. Deriche, "Vector-valued image regularization with PDEs: A common framework for different applications," *IEEE Trans. Pattern Anal. Mach. Intell.*, vol. 27, no. 4, pp. 506–517, Apr. 2005.
[46] J. Weickert and H. Scharr, "A scheme for coherence-enhancing diffusion filtering with optimized rotation invariance," *J. Visual Commun. Image Rep.*, vol. 13, no. 1–2, pp. 103–118, Mar. 2002.
[47] M. N. Do and M. Vetterli, "The contourlet transform: An efficient directional multiresolution image representation," *IEEE Trans. Image Process.*, vol. 14, no. 12, pp. 2091–2106, Dec. 2005.
[48] M. Vetterli, "Multidimensional subband coding: Some theory and algorithms," *IEEE Trans. Signal Process.*, vol. 6, no. 2, pp. 97–112, Apr. 1984.
[49] M. A. Savelonas, E. A. Mylona, and D. Maroulis, "Unsupervised 2D gel electrophoresis image segmentation based on active contours," *Pattern Recognit.*, vol. 45, no. 2, pp. 720–731, Feb. 2012.
[50] L. I. Rudin, S. Osher, and E. Fatemi, "Nonlinear total variation based noise removal algorithms," *Physica D*, vol. 60, no. 1–4, pp. 259–268, 1992.
[51] M. Nikolova, M. K. Ng, and C. P. Tam, "Fast nonconvex nonsmooth minimization methods for image restoration and reconstruction," *IEEE Trans. Med. Imag.*, vol. 19, no. 12, pp. 3073–3088, Dec. 2010.
[52] C. Li. (2011). *University of Connecticut* [Online]. Available: http://www.engr.uconn.edu/˜cmli/
[53] X. Bresson. (2010). *City University of Hong Kong* [Online]. Available: http://www.cs.cityu.edu.hk/˜xbresson/
[54] [Online]. Available: http://www.mathworks.com/matlabcentral/fileexchange/22410-rof-denoising-algorithm
[55] [Online]. Available: http://www.math.hkbu.edu.hk/˜mng/
[56] D. D.-Y. Po and M. N. Do, "Directional multiscale modeling of images using the contourlet transform," *IEEE Trans. Image Process.*, vol. 15, no. 6, pp. 1610–1620, Jun. 2006.
[57] P. Arbelaez, M. Maire, C. Fowlkes, and J. Malik, "Contour detection and hierarchical image segmentation," *IEEE Trans. Pattern Anal. Mach. Intell.*, vol. 33, no. 5, pp. 898–916, May 2011.
[58] A. K. Mishra, P. W. Fieguth, and D. A. Clausi, "Decoupled active contour (DAC) for boundary detection," *IEEE Trans. Pattern Anal. Mach. Intell.*, vol. 33, no. 2, pp. 310–324, Feb. 2011.
[59] L. Bertelli, B. Sumengen, B. S. Manjunath, and F. Gibou, "A variational framework for multiregion pairwise-similarity-based image segmentation," *IEEE Trans. Pattern Anal. Mach. Intell.*, vol. 30, no. 8, pp. 1400–1414, Mar. 2008.
[60] J. M. Geusebroek, G. J. Burghouts, and A. W. M. Smeulders, "The Amsterdam library of object images," *Int. J. Comput. Vis.*, vol. 61, no. 1, pp. 103–112, 2005.
[61] [Online]. Available: http://www.cancerimagingarchive.net
[62] T. Eckhard, E. M. Valero, and J. L. Nieves, "Labial teeth and gingiva color image segmentation for gingival health-state assessment," in *Proc. Eur. Conf. CGIV*, 2012, pp. 102–107.
[63] W. R. Crum, O. Camara, and D. L. G. Hill, "Generalized overlap measures for evaluation and validation in medical image analysis," *IEEE Trans. Med. Imag.*, vol. 25, no. 11, pp. 1451–1461, Nov. 2006.
[64] B. Mory and R. Ardon, "Fuzzy region competition: A convex two-phase segmentation framework," in *Scale Space and Variational Methods in Computer Vision*, vol. 4485. Berlin, Germany: Springer, 2007, pp. 214–226.

Eleftheria A. Mylona received the B.Sc. degree in applied mathematical and physical sciences from the National Technical University of Athens, Athens, Greece, the M.Sc. degree in physics from the University of Edinburgh, Scotland, U.K., and the Ph.D. degree in image analysis from the University of Athens, Athens, Greece, in 2006, 2007, and 2014, respectively.

Currently, she is affiliated with the Institute for Astronomy, Astrophysics, Space Applications and Remote Sensing, National Observatory of Athens, Athens, Greece. She has co-authored 16 research articles on biomedical image analysis. Her current research interests include pattern recognition and image analysis.

Ms. Mylona received a scholarship co-financed by the European Union and Greek National funds during the Ph.D. research.

Michalis A. Savelonas (M'08) received the B.Sc. degree in physics, the M.Sc. (Hons.) degree in cybernetics, and the Ph.D. (Hons.) degree in the area of image analysis from the University of Athens, Athens, Greece, in 1998, 2001, and 2008, respectively.

Among positions in various academic institutions, including University of Athens, University of Houston, TX, USA, Hellenic Air Force Academy and Technological and Educational Institute of Lamia, he is currently a Research Fellow with Athena Research and Innovation Center, Xanthi, Greece. He has co-authored over 50 research articles and book chapters, and has been actively involved in several EU, US and Greek Research and Development projects. From 2002 to 2004, he was with software industry for the development of real-time systems. His current research interests include image analysis, segmentation, pattern recognition, bioinformatics, and watermarking.

Dr. Savelonas received a scholarship from the Greek General Secretariat of Research and Technology and the European Social Fund for the Ph.D. research. He is a Reviewer in prestigious international journals including IEEE TRANSACTIONS ON IMAGE PROCESSING and PATTERN RECOGNITION.

Dimitris Maroulis (M'02) received the B.Sc. degree in physics, the M.Sc. degree in Radioelectricity (Hons.), the M.Sc. degree in Cybernetics, and the Ph.D. (Hons.) degree in computer science, all from the University of Athens, Athens, Greece.

He served as a Research Fellow for 3 years at the Space Research Department of Meudon Observatory, Paris, France, and afterwards, he collaborated for over 10 years with the same Department. He was with the Hellenic Telecommunications Organization (PTT, Department of Statistics) for 2 years. He served as Lecturer, Assistant and Associate Professor at the Departments of Physics and Informatics of the University of Athens. Currently, he is a Professor at the same University and leader of the Real-Time Systems and Image Analysis Lab (RTS-image). He has over 20 years of experience in the areas of data acquisition and real-time systems, and over 15 years of experience in the area of image/signal analysis and processing. He has also been collaborating with many Greek and European hospitals and health centers for over 15 years in the field of biomedical informatics. He has been actively involved in over 12 European and National Research and Development projects and has been the Project Leader of five of them, all in the areas of image/signal analysis and real-time systems. He has published over 150 research papers and book chapters, and currently, there are over 1400 citations that refer to his published work. He has made peer reviews for over 12 international journals, as well as for an equal number of international conferences. His current research interests include data acquisition and real-time systems, pattern recognition, image analysis, with applications on biomedical systems, and bioinformatics.

This article has been accepted for inclusion in a future issue of this journal. Content is final as presented, with the exception of pagination.

Automated Adjustment of Region-Based Active Contour Parameters Using Local Image Geometry

Eleftheria A. Mylona, Michalis A. Savelonas, *Member, IEEE*, and Dimitris Maroulis, *Member, IEEE*

***Abstract*—A principled method for active contour (AC) parameterization remains a challenging issue in segmentation research, with a potential impact on the quality, objectivity, and robustness of the segmentation results. This paper introduces a novel framework for automated adjustment of region-based AC regularization and data fidelity parameters. Motivated by an isomorphism between the weighting factors of AC energy terms and the eigenvalues of structure tensors, we encode local geometry information by mining the orientation coherence in edge regions. In this light, the AC is repelled from regions of randomly oriented edges and guided toward structured edge regions. Experiments are performed on four state-of-the-art AC models, which are automatically adjusted and applied on benchmark datasets of natural, textured and biomedical images and two image restoration models. The experimental results demonstrate that the obtained segmentation quality is comparable to the one obtained by empirical parameter adjustment, without the cumbersome and time-consuming process of trial and error.**

***Index Terms*—Active contours, automated parameterization, structure tensors.**

I. Introduction

ACTIVE contours (ACs) are a rather mature image segmentation paradigm, with several variations proposed in literature [1]–[4]. However, their parameterization remains a challenging, open issue, with strong implications on the quality, objectivity, and robustness of the segmentation results. Very often, parameters are empirically adjusted on a trial and error basis, a process which is laborious and time-consuming, based on subjective as well as heuristic considerations. On one hand, nonexpert users such as medical doctors (MDs) and biologists require technical support since they are not familiar with the algorithmic inner mechanisms. On the other hand, parameter configurations of image analysis experts are usually suboptimal and applicable to specific datasets [5]. Moreover, the proliferation of AC variations raises the need for a framework facilitating fair comparisons.

Tracing the main line of progress in AC literature, one can observe that the parameterization issue persists. The first AC model, widely known as the snake model, has been proposed in the seminal work of Kass *et al*. [6]. The snake model employed physically-inspired terms for contour stiffness and rigidity, as well as image-derived terms, all weighted by empirically adjusted parameters. The snake model was succeeded by the geodesic AC model (GAC) [7]–[11] which, unlike its predecessor, is topologically adaptable and employs intrinsic contour representations instead of 1-D parameterized curves. However, GAC is still empirically parameterized. In the course of the evolution of the AC paradigm in the following years, which included edge-based [12]–[17], region-based [18]–[27] and hybrid models [28]–[33], the need for empirical parameter adjustment remained.

Numerous approaches have been proposed in order to cope with the issue of parameterization. Pluempitiwiriyawej *et al*. [34] and Tsai *et al*. [35] dynamically update AC parameters as contour evolves. This temporal dependency may lead to the propagation of early errors in the later contour evolution stages. In addition, in these approaches parameters are not spatially-varying, failing to capture local image features. Kokkinos *et al*. [36] proposed a statistical approach employing the posterior probabilities of texture, edge and intensity cues as contour weights in a locally adaptive manner. Nevertheless, their approach still requires technical skills by the domain user. Keuper *et al*. [37] and Liu *et al*. [38] presented a method for dynamic adjustment of AC parameters, applicable on the detection of cell nuclei and lip boundaries, respectively. Both methods require a priori knowledge considering the shape of the target region. Iakovidis *et al*. [39] and Hsu *et al*. [40] introduced a framework for optimization of AC parameters based on genetic algorithms. However, these heuristic approaches converge slowly in locally optimal solutions. Allili and Zhou [41] proposed an approach for estimating hyper-parameters capable of balancing the contribution of boundary and region-based terms. In their approach, empirical parameter tuning is still involved. Yushkevich *et al*. [42] developed an application for level-set segmentation of images of anatomical structures. Although their GUI is friendly to nonexpert users, parameter settings are still empirically fixed.

Manuscript received July 29, 2013; revised December 22, 2013; accepted March 28, 2014. This work was supported in part by the European Union (European Social Fund-ESF) and in part by the Greek National Funds through the Operational Program “Education and Lifelong Learning” of the National Strategic Reference Framework (NSFR)-Research Funding Program: Heracleitus II. Investing in knowledge society through the European Social Fund. This paper was recommended by Associate Editor H. Lu.

The authors are with the Realtime Systems and Image Analysis Group, Department of Informatics and Telecommunications, National and Kapodistrian University of Athens, Athens 15703, Greece (e-mail: emylona@di.uoa.gr; msavel@di.uoa.gr; dmaroulis@di.uoa.gr).

Color versions of one or more of the figures in this paper are available online at http://ieeexplore.ieee.org.

Digital Object Identifier 10.1109/TCYB.2014.2315293

This paper introduces a novel framework for automated adjustment of region-based AC regularization and data fidelity parameters based on local image geometry information. Starting from the observation that these parameters and the eigenvalues of structure tensors are associated with the same orthogonal directions, we encode local image geometry by mining the orientation coherence in edge regions. The latter can be encoded by means of orientation entropy (OE), a measure which is an increasing function of orientation variability of edges, obtaining low values in structured regions containing edges of similar orientations and high values in unstructured regions containing edges of multiple orientations. As a result, those forces that guide contour away from randomly oriented, high-entropy edge regions are amplified and iterations dedicated to erroneous local minima are avoided, speeding up contour convergence. On the other hand, forces imposed within the proximity of structured edges, naturally related to target edge regions, are reduced, enhancing segmentation accuracy. Preliminary variations of this paper have appeared in [43] and [44]. Even though these variations obtained promising segmentation results, they were only applied on a limited number of images.

It should be highlighted that the aim of this paper is to introduce a framework for automatically adjusting region-based AC parameters, rather than presenting yet another AC model. Moreover, the convergence acceleration is a byproduct of the proposed framework and not its main motivation, which is the capability of AC self-parameterization.

The contribution of the proposed framework has several aspects.

1) It is unsupervised and may be treated as a "black box": the regularization and data fidelity parameters are automatically adjusted. Hence, technical skills are not a prerequisite for the domain user and he/she is completely released from the tedious and time-consuming process of trial and error adjustment. In addition, the subjectivity of the results is reduced.
2) It is applicable to several types of images: it can be applied to natural, textured and biomedical images as well as to real-world photographs.
3) It does not require any a priori knowledge or learning considering the shape/size of the target region.
4) It guides contour away from high-entropy edge regions in order to avoid iterations dedicated to erroneous local minima, by selectively amplifying data fidelity forces.

To the best of our knowledge, this is the first paper for automated region-based AC parameterization of regularization and data fidelity energy terms combining the above elements.

The remainder of this paper is organized as follows. Section II presents the motivation behind the idea of the proposed framework, as well as its details. Section III demonstrates the results and comparisons obtained by experiments with four state-of-the-art region-based AC models and two image restoration models, which minimize an energy functional consisting of regularization and data fidelity terms. Conclusion and future research directions are summarized in Section IV.

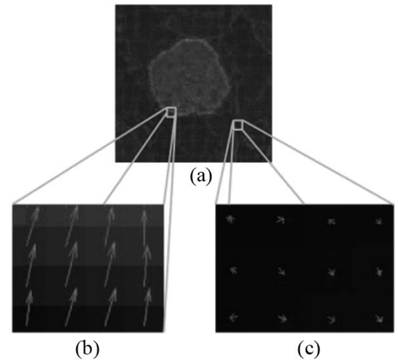

Fig. 1. (a) Structure tensor field of a test image. (b) Zoomed-in view of region which corresponds to a target edge region. (c) Zoomed-in view of region which corresponds to a nontarget edge region.

II. Proposed Framework

A. Motivation

Overviews of the standard formalisms of the most prominent AC variations can be found in [19] and [26]. The proposed framework is motivated by the attractive properties of structure tensor eigenvalues [45]. The latter are capable of describing the orientation coherence in edge regions. An edge region containing edges of similar orientations is characterized as a structured edge region, whereas an edge region containing multiple orientations is characterized as an unstructured one.

Structured edge regions correspond to target edges. This is illustrated in Fig. 1, which shows: 1) the structure tensor field of a test image; 2) a zoomed region which corresponds to a target edge region; and 3) a zoomed region which corresponds to a nontarget edge region. In the case of Fig. 1(b), the target edge region is characterized by edges of similar orientations, whereas in the case of Fig. 1(c), the nontarget edge region is associated with multiple orientations. Based on the above remark, structure tensor eigenvalues are capable of identifying whether an edge region is target or nontarget, depending on the variability of the orientations of its edges.

According to Weickert's diffusion model [46], a structure tensor D is defined as follows:

$$D = \nabla I \otimes \nabla I = \nabla I \cdot \nabla I^T \tag{1}$$

where I is an image. D has an orthonomal basis of eigenvectors v_1, v_2 with $v_1 || \nabla I$, $v_2 \perp \nabla I$ and λ_1, λ_2 are the corresponding eigenvalues defined as follows:

$$\lambda_{1,2} = \frac{1}{2}(I_{xx} + I_{yy} \pm \sqrt{(I_{xx} - I_{yy})^2 + 4I_{xy}^2} \tag{2}$$

where the + sign belongs to λ_1. The principal eigenvalue λ_1 is longitudinal with respect to the principal axis of the elliptical tensor, whereas the minor eigenvalue λ_2 is vertical with respect to the same principal axis.

Region-based ACs very often conform to Euler–Lagrange equations which consist of regularization and data fidelity terms [19]. Regularization terms are longitudinal to contour direction whereas data fidelity terms are vertical, attracting contours toward the boundaries of target edge regions. It is tempting to notice that the regularization weight, denoted as

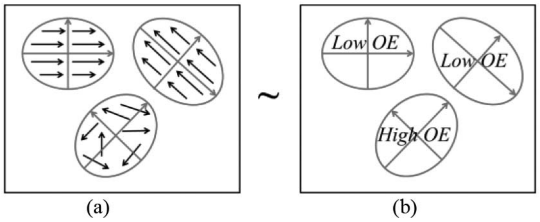

Fig. 2. Schematic representation of (a) elliptical structure tensors (red ellipses) consisting of regions of single and multiple orientations (black arrows) and (b) OE behavior on each structure tensor.

w_{reg}, corresponds to the same direction as the eigenvalue of the horizontal eigenvector of a structure tensor. Similarly, the data fidelity weight, denoted as w_{df}, corresponds to the same direction as the eigenvalue of the vertical eigenvector. This isomorphism indicates a link between the regularization and data fidelity terms and the eigenvalues of structure tensors.

B. Orientation Coherence Estimation

Motivated by the above observations, the proposed framework adjusts regularization and data fidelity parameters automatically, in a similar fashion to Weickert's diffusion model, in order to describe the orientation coherence of edge regions. The latter is calculated by orientation entropy (OE) defined as follows:

$$OE_{jk} = -\sum_{n=1}^{N_{jk}} \sum_{m=1}^{M_{jk}} p_{jk}(m,n) \cdot \log p_{jk}(m,n) \tag{3}$$

$$p_{jk} = \frac{|I_{jk}(m,n)|^2}{\sqrt{\sum_{n=1}^{N_{jk}} \sum_{m=1}^{M_{jk}} [I_{jk}(m,n)]^2}} \tag{4}$$

where I_{jk} is the subband image generated by a multidirectional filtering method such as the contourlet transform (CT) [47], OE_{jk} is the OE of the subband image I_{jk} in the k^{th} direction and the j^{th}level, M_{jk} is the row size and N_{jk} the column size of the subband image.

OE obtains high values in cases of unstructured edge regions, which are associated with noise and artifacts and low values in cases of structured edge regions, which are associated with target edges. Fig. 2(a) depicts a schematic representation of elliptical structure tensors (red ellipses) consisting of regions of single and multiple orientations (black arrows), whereas Fig. 2(b) depicts the respective OE behavior on each structure tensor.

Each $q \times q$ image grid is fed into CT through an iterative procedure. The size of the $q \times q$ image grid is experimentally determined as the minimum of the negative power of two of the original image size, which still maintains at least an edge region. For instance, in the case of the thyroid ultrasound images used in the experiments presented in Section III, it has been found that for an image of 320×320, an image grid of 40×40 ($40 = 320 \times 2^{-3}$) is suitable. The image grid is further decomposed into two pyramidal levels, which are then transformed into four directional subbands: 0°, 45°, 90°, and 135° in order to investigate whether the edge region of the grid is a target or a nontarget edge region.

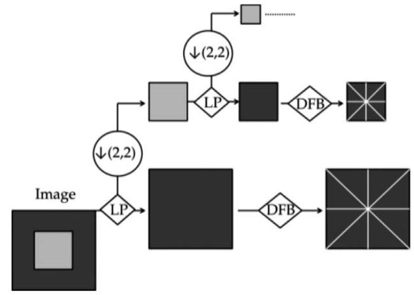

Fig. 3. CT filter-bank. LP provides a down-sampled low-pass and a band-pass version of the image. Consequently, a DFB is applied to each band-pass image.

The band-pass directional subbands represent the local image structure and apart from intensity, also hold textural information. CT provides an inherent multiscale filtering mechanism, capable of filtering out randomly oriented edges associated with noise, artifacts and/or background clutter. Moreover, CT is directly implemented in the discrete domain and is capable to selectively represent edges of various scales and directions. Small scale edges are associated with noise or artifacts.

C. Contourlet Transform (CT) [47]

Aiming at a sparse image representation, CT employs a double iterated filter-bank, which captures point discontinuities by means of the Laplacian pyramid (LP) and obtains linear structures by linking these discontinuities with a directional filter-bank (DFB). The final result is an image expansion that uses basic contour segments. Fig. 3 illustrates a CT iterated filter-bank.

The downsampled low-pass and band-pass versions of the image contain lower and higher frequencies, respectively. It is evident that, the band-pass image contains detailed information of point discontinuities, which are associated with target edge regions. Furthermore, DFB is implemented by an l-level binary tree which leads to 2^l subbands. In the first stage, a two-channel quincunx filterbank [48] with fan filters divides the 2-D spectrum into vertical and horizontal directions. In the second stage, a shearing operator reorders the samples. As a result, different directional frequencies are captured at each decomposition level. The number of iterations depends mainly on the size of the input image. The total number of directional subbands K_{total} is calculated as

$$K_{total} = \sum_{j=1}^{J} K_j \tag{5}$$

where K_j is a subband DFB applied at the j^{th} level ($j = 1, 2, \ldots, J$). Fig. 4 depicts the CT filter-bank of a sampled image grid, decomposed to the finest and second finest scales, which are partitioned into four directional subbands.

Among the OE values calculated for each subband, the maximum OE value of the most informative scale j and direction k, which depends on N and M is calculated and assigned to all pixels of each grid. The result is considered as an OE matrix reflecting local structure information.

This article has been accepted for inclusion in a future issue of this journal. Content is final as presented, with the exception of pagination.

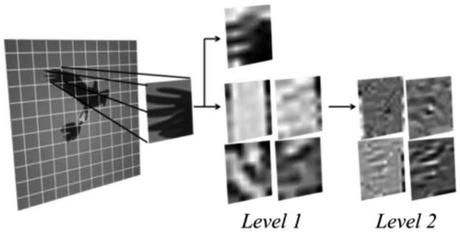

Fig. 4. CT filter-bank of a sample grid decomposed to two levels of LP and four band-pass directional subbands.

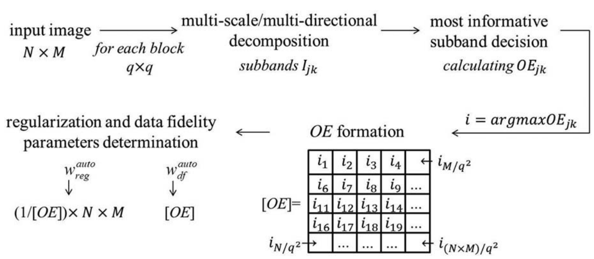

Fig. 5. Block diagram of the pipeline of the proposed framework.

D. Automated Parameterization

The regularization parameter w_{reg} and the data fidelity parameter w_{df} are matrices of the same dimensions as the original image and are calculated according to the following equations:

$$w_{reg} = (1/w_{df}) \times N \times M, \quad w_{df} = \arg_{I_{jk}} \max(OE(I_{jk})). \quad (6)$$

In cases of regions of randomly oriented edges, high values are assigned to w_{df}, amplifying data fidelity forces in the early stages of contour evolution. In such cases, contour will be repelled from the regions of randomly oriented, unstructured edges and iterations dedicated to false local minima, associated with such edges will be avoided. It should be highlighted that both parameters are calculated only once. The aim is to navigate the contour directly to structured edge regions, already from the early stages of evolution and to hinder erroneous behavior, by "constantly reminding" the locations of structured edge regions. Moreover, apart from separately adjusting each parameter, the proposed framework also achieves a balanced trade-off between regularization and data fidelity parameters. In cases of unstructured edge regions, as quantified by the maximum value of OE over all sub-band images, data provide a less reliable clue than contour regularization. On the other hand, in structured edge regions, data provide a more reliable clue. Both cases of high and low maximum OE, as well as cases with intermediate values of OE are addressed by setting regularization terms as the reciprocal of data fidelity terms.

The two spatially-varying matrices representing the automatic regularization and data fidelity parameters are integrated into the Euler–Lagrange equation, replacing the empirically determined uniform parameters. The pipeline of the proposed framework is portrayed in the block diagram of Fig. 5.

III. Results

The proposed framework has been embedded into four region-based AC models [17], [19], [26], [49] consisting of regularization and data fidelity energy terms, in order to evaluate the segmentation performance of automated versus empirical parameterization. Additionally, the proposed framework has been integrated into the Rudin–Osher–Fatima (ROF) model [50] and the Nikolova *et al.* model [51] for image restoration, so as to test its effectiveness on alternative inverse problems irrespective of the application. The well-known Chan–Vese model [19] and the model of Savelonas *et al.* [49] have been implemented in MATLAB, whilst MATLAB codes of the models of Li *et al.* [17], Bresson *et al.* [26], the ROF model [50], and the Nikolova *et al.* model [51] can be downloaded from the authors' homepages [52], [53], [54], and [55], respectively. The "9-7" biorthogonal filter for the multiscale and multidirectional decomposition stage of CT is applied [56].

The results of the original, empirically parameterized algorithms were compared to those obtained by the automated versions. Apart from the experiments on the Berkeley segmentation dataset [57] and test images obtained by various datasets [58], [59], additional experiments were conducted on 20 images of the Amsterdam library of object images (ALOI) database [60], 20 coronal scans of the lung image database consortium and image database resource initiative (LIDC-IDRI) [61], 20 thyroid ultrasound images containing hypoechoic nodules over a noisy background, provided by the radiology department of Euromedica S.A., Greece and 20 images of the labial teeth and gingiva photographic image database (LTG-IDB) [62], in order to evaluate the proposed framework on large benchmark datasets. All medical images used were investigated by MDs who provided ground truth images, whereas contour initialization was the same for both the proposed framework and the empirically fine-tuned version, in order to facilitate fair comparisons.

It should be stressed that, rather than comparing one AC method with another, the experiments to follow aim to evaluate the effectiveness of the proposed framework by examining whether the segmentation performance of the unsupervised version is at least comparable to the one obtained by the empirically fine-tuned version.

Fig. 6 illustrates: (a) and (b) test images obtained by the Berkeley dataset, (c) a thyroid ultrasound (US) test image containing a nodule, (a_1), (b_1), and (c_1) ground-truth images and (a_2), (b_2), and (c_2) segmentation results of the proposed framework. Aiming to evaluate the obtained results, the region overlap measure, known as the Tannimoto Coefficient (TC) [63], is considered

$$TC = \frac{N(A \bigcap B)}{N(A \bigcup B)} \quad (7)$$

where A is the region delineated by the segmentation method under evaluation, B is the ground truth region and $N()$ indicates the number of pixels of the enclosed region. The results of Fig. 6(a_2), (b_2), and (c_2) correspond to TC values of 90.3%, 88.7% and 91.4%, respectively.

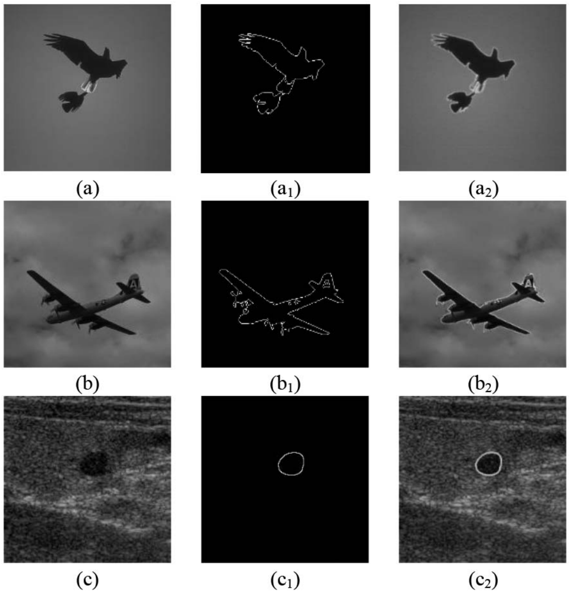

Fig. 6. Segmentation based on local image geometry. (a)–(c) Original test images. (a_1)–(c_1) Ground-truth images. (a_2)–(c_2) Segmentation results of the proposed framework.

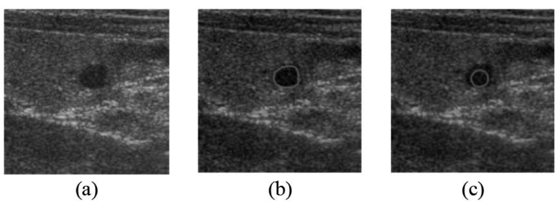

Fig. 7. (a) Sample image. (b) Segmentation results obtained by the empirically fine-tuned version ($w_{reg}^{fixed} = 0.006 \cdot 255^2$, $w_{df}^{fixed} = 1$). (c) Segmentation results obtained by the randomly-tuned version ($w_{reg}^{fixed} = 0.001 \cdot 255^2$, $w_{df}^{fixed} = 0.1$). Size 256 × 256.

Aiming at highlighting the significance of the proposed framework, we have investigated the sensitivity of the Chan–Vese model to small alterations of parameters. Except of being adjusted with parameters determined as optimal, the empirical version of the Chan–Vese model is also adjusted with parameters which are randomly set and is tested on sample images obtained by the utilized datasets. Accordingly, w_{reg}^{fixed} and w_{df}^{fixed} were set to randomly selected values, which fluctuated up to 10% from the optimal ones. Fig. 7 depicts: (a) a sample image, (b) segmentation results obtained by the empirically fine-tuned Chan–Vese model, and (c) segmentation results obtained by randomly tuning the same model, where w_{reg}^{fixed} and w_{df}^{fixed} were randomly set to $0.001 \cdot 255^2$ and 0.1, respectively. It is evident that, the segmentation results obtained by the random tuning differ significantly from the ones obtained by empirical fine-tuning. Random tuning leads to an average TC value of 58.3 ± 1.7%, whereas empirical fine-tuning leads to an average TC value of 82.0 ± 1.5% with respect to all images tested. A similar behavior has been observed to the rest of the AC applications presented. Hence, ACs are sensitive even to small alterations of parameters and the segmentation results are highly dependent on the "optimality" of the empirical fine-tuning thus, on the technical skill of the end-user. On the contrary, the proposed framework achieves a high segmentation quality, comparable to the segmentation quality obtained by empirically fine-tuning, but in an automated fashion, endowing segmentation results with objectivity.

In the experiments to follow, evolution is stopped when the overlap between all pairs of regions enclosed by AC instances of the last five successive iterations, is more than 99.95%, as quantified by TC.

A. *Chan–Vese Model [19]*

The Chan–Vese model determines the level set evolution by solving the following equation

$$\frac{\partial \phi}{\partial t} = w_{reg}^{fixed} \cdot \delta(\phi(x,y)) \cdot div\left(\frac{\nabla \phi}{|\nabla \phi|}\right) - w_{df}^{fixed}(I(x,y) - c_1)^2 + w_{df}^{fixed}(I(x,y) - c_2)^2 \tag{8}$$

where ϕ is the level set function, I the observed image, c_1, c_2 the average intensities inside and outside of the contour, respectively, w_{reg}^{fixed} the fixed regularization parameter and w_{df}^{fixed} the fixed data fidelity parameter. The latter are assigned the same value as suggested by Chan and Vese. For the empirical case, the optimal parameters are set according to the original paper [19]. For the proposed framework, the regularization and data fidelity parameters are automatically calculated according to (6).

The segmentation performance of the Chan–Vese model for both empirically and automatically parameterized versions is evaluated on test images obtained by [58] and [59]. The test images contain a foreground object of interest over an inhomogeneous background. The contour is initialized as a closed circle with the same center and radius for all test images and for both empirically and automatically parameterized versions, so as to ensure consistency.

Fig. 8 illustrates the contour obtained on two test images, for the second as well as for the final iteration. The first image contains an object of interest of high average intensity over a darker background, whereas the second image contains a dark object of interest over a brighter background. Yellow color is used for the initial contour in both versions whereas blue and green colors are used for the contours obtained by the empirical and automated version, on the second and final iteration.

The dilation operator has been used to morphologically reconstruct contours and enhance image appearance. In the case of the first image, the automated version converges faster to the object boundaries since the forces guiding contour evolution are appropriately amplified in nontarget, high-entropy edges. In the case of the second image, the empirical version is delayed on the fine image details and converges to erroneous boundaries. This can be explained by the gross nature of the Chan–Vese model, which is guided by region-based forces and thus, is delayed on erroneous local intensity minima associated with brighter background clutter. On the contrary, the automated version is guided by region-based forces, as well as by local geometry information, incorporated in the parameters matrices and is capable to identify the actual target edge regions.

This article has been accepted for inclusion in a future issue of this journal. Content is final as presented, with the exception of pagination.

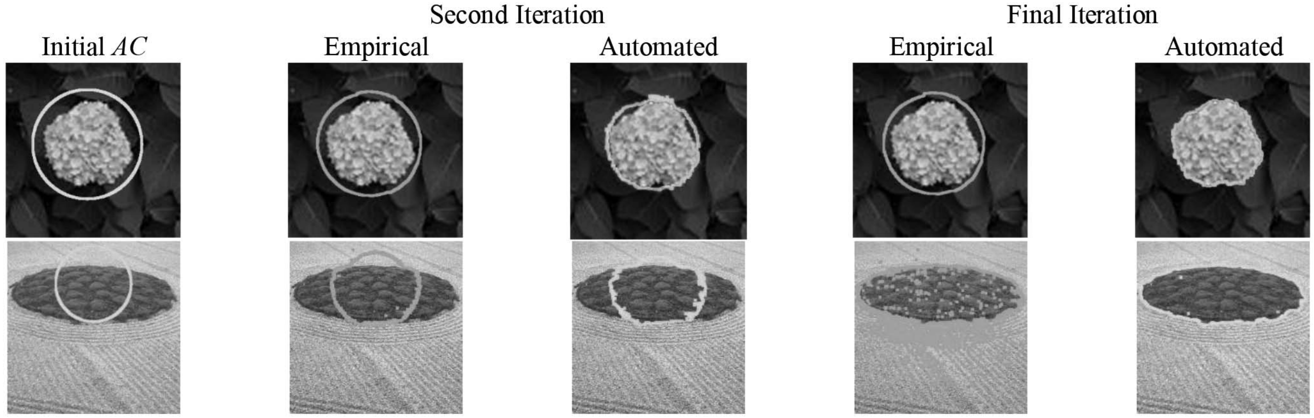

Fig. 8. Examples of contour evolution of the Chan–Vese model. Yellow color is used for the initial contour in both versions; blue and green colors are used for the contours obtained by the empirical ($w_{reg}^{fixed} = 0.006 \cdot 255^2$, $w_{df}^{fixed} = 1$) and automated version, respectively. Size 320×320.

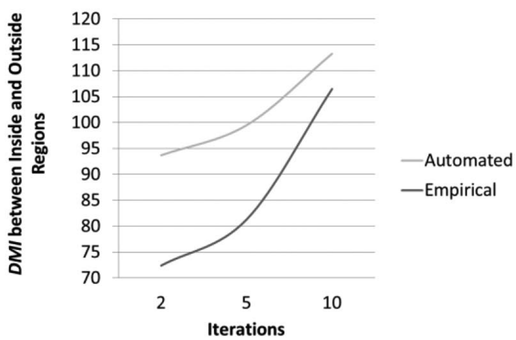

Fig. 9. DMI calculated for the early stages of evolution of the automated versus empirical version of the Chan–Vese model, presented in Fig. 8.

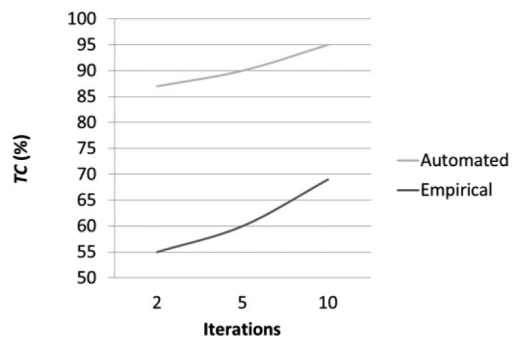

Fig. 10. TC for the early stages of evolution of automated versus empirical version presented in Fig. 8.

Aiming to evaluate the convergence rate of both versions, we define the difference of mean intensity values (DMI) between inside and outside region terms and implement the following algorithm.

$\forall$ iteration i

1. Calculate inside $|I(x, y) - c_1|^2$ and outside $|I(x, y) - c_2|^2$ region terms.
2. Normalize and quantize both terms in the range [0, 255].
3. Calculate mean values.
4. Calculate DMI.

Fig. 9 depicts DMI calculated for the early stages of evolution of the empirical and automated versions of the Chan–Vese model presented in Fig. 8. It can be observed that DMI reaches higher values in the automated case in the early stages of contour evolution. Again, this is explained by the fact that the forces guiding contour evolution are appropriately amplified in nontarget edges. Fig. 10 compares the segmentation performance of the empirical and automated version for the early stages of evolution in terms of TC.

It should be mentioned that the proposed framework is potentially applicable on similar methods which are capable of solving two-phase segmentation problems, as is the case with the model of Mory *et al*. [64].

B. Bresson et al. Model [26]

Bresson *et al*. propose to minimize the following energy functional based on the Chan–Vese model [19], in order to carry out the global minimization of segmentation

$$E(u, c_1, c_2, w_{df}^{fixed}) = TV_g(u) + w_{df}^{fixed} \int_{\Omega} (c_1 - I(x))^2 - (c_2 - I(x))^2 dx \quad (9)$$

where u is a characteristic function 1_{Ω_C} of a closed set where C denotes the nonconnected boundaries of Ω_C, g an edge-indicator function, $TV_g(u)$ the weighted total variation (TV) energy of the function u with the weight function g, i.e., $TV_g(u) = \int g(x)|\nabla u|dx$, and w_{df}^{fixed} the fixed data fidelity parameter. For the empirical case, the latter is set according to the original paper [26]. For the proposed framework, the data fidelity parameter is automatically calculated according to (6).

The model of Bresson *et al*. [26] is evaluated on test images obtained by the first author's homepage. Fig. 11 presents segmentation results for *Cheetah* and *Zebra* textured images. The final contour satisfies

$$\left\{(x, y) \in \Omega | I^{final}(x, y) > 0.5\right\}. \quad (10)$$

Magenta and green colors correspond to empirical and automated version, respectively. It is evident that both versions

This article has been accepted for inclusion in a future issue of this journal. Content is final as presented, with the exception of pagination.

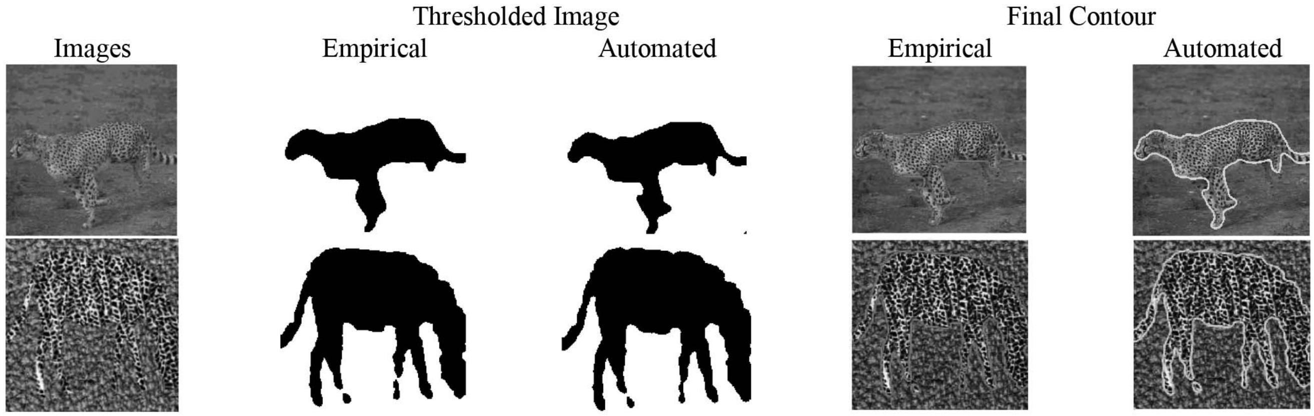

Fig. 11. Segmentation results of the model of Bresson *et al*. Magenta and green contours correspond to empirical ($w_{reg}^{fixed} = 0.7$, $w_{df}^{fixed} = 0.4$) and automated parameterization, respectively. Size 320×320.

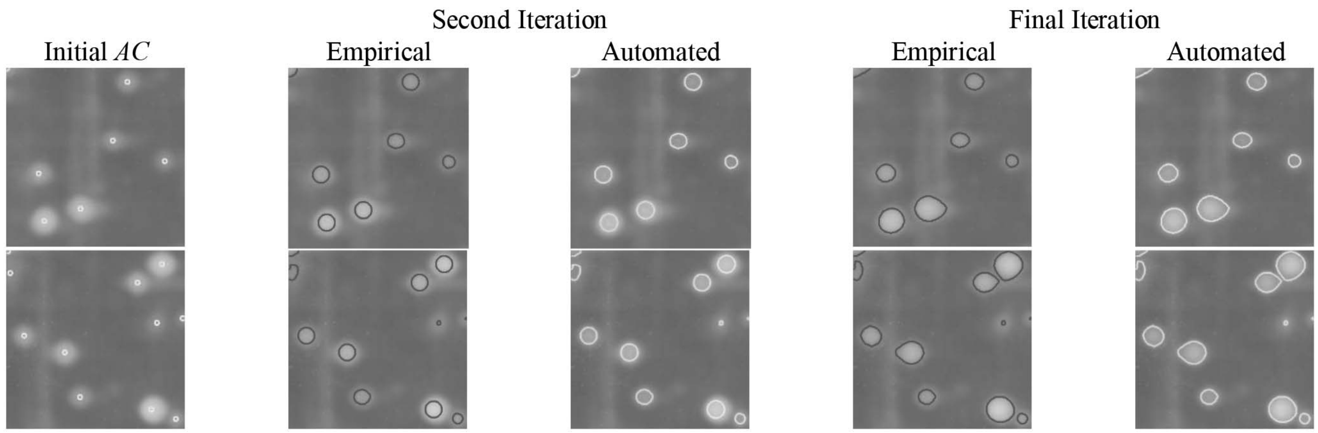

Fig. 12. Segmentation results of the model of Savelonas *et al*. Yellow is used for the initial contour in both versions, purple and green contours correspond to empirical ($w_{reg}^{fixed} = 0.006 \cdot 255^2$, $w_{df}^{fixed} = 1$) and automated parameterization, respectively. Size 320×320.

converge to the actual object boundaries, resulting in comparable segmentation accuracy. It should be pointed out that the empirical version of the model of Bresson *et al*. convexifies energy in order to compute a global minimizer. The automated version captures local geometry information correctly and converges to the actual target edge regions.

C. Savelonas et al. Model [49]

The region-based AC in Savelonas *et al*. model converges based on the Chan–Vese model [19] according to the following equation:

$$\begin{aligned}\frac{\partial\phi}{\partial t} = w_{reg}^{fixed} \cdot \delta(\phi(x,y)) \cdot div\left(\frac{\nabla\phi}{|\nabla\phi|}\right)\\ -w_{df_1}^{fixed}(I_1(x,y)-c_1)^2 + w_{df_1}^{fixed}(I_1(x,y)-c_2)^2\\ -w_{df_2}^{fixed}(I_2(x,y)-c_3)^2 + w_{df_2}^{fixed}(I_2(x,y)-c_4)^2\end{aligned} \quad (11)$$

where ϕ is the level set function, I_1, I_2 the observed image and the binarized image which is the output of morphological processing, respectively, c_1, c_2 and c_3, c_4 the average intensities inside and outside of the contour of I_1 and I_2, respectively, w_{reg}^{fixed} the fixed regularization parameter, $w_{df_1}^{fixed}$ and $w_{df_2}^{fixed}$ the fixed data fidelity parameters of I_1 and I_2, respectively. For the empirical case, the optimal parameters are set according to the original paper [49]. For the proposed framework, the regularization and data fidelity parameters are automatically calculated according to (6). The segmentation performance of the recent model of Savelonas *et al*. for both empirical and automated versions is evaluated on real 2-D gel electrophoresis (2D-GE) images, obtained by the Biomedical Research Foundation of the Academy of Athens.

Fig. 12 illustrates contours obtained on the second as well as on the final iteration, for 2D-GE sub-images. Yellow color is used for the initial contour in both versions, whereas purple and green colors correspond to empirical and automated version, respectively. It is evident that the segmentation results of the empirical and automated versions are comparable. Nonetheless, as already pointed out, empirical parameterization requires tedious, time-consuming experimentation. Our framework is capable of obtaining comparable results in an automated fashion. Fig. 13 depicts DMI for both versions, for the early stages of contour evolution presented in Fig. 12. Again in the case of the automated version, DMI is slightly higher in early iterations.

In Fig. 14, the comparison is performed in terms of TC, providing a quantification of the actual segmentation performance for the early stages of evolution. So far, the proposed framework has been applied on region-based AC models.

This article has been accepted for inclusion in a future issue of this journal. Content is final as presented, with the exception of pagination.

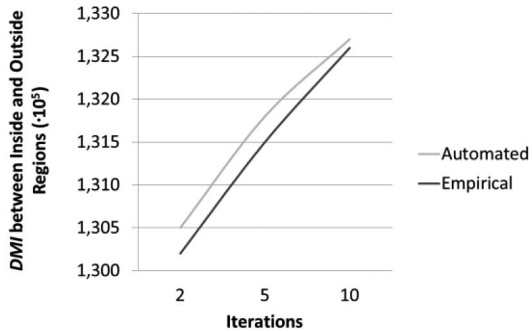

Fig. 13. DMI between inside and outside regions for the early stages of evolution of automated versus empirical version presented in Fig. 12.

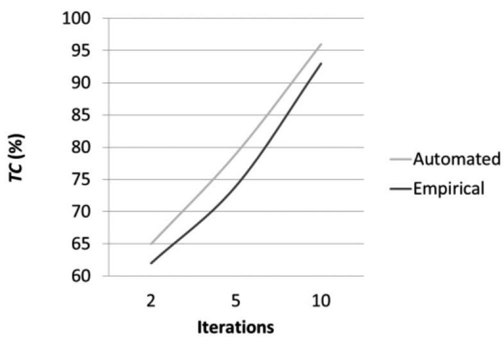

Fig. 14. TC for the early stages of evolution of automated versus empirical version presented in Fig. 12.

D. Li et al. Model [17]

The proposed framework has also been applied on the model of Li *et al*. so as to investigate its effectiveness on AC models which are not purely region-based, with respect to data fidelity and regularization parameters. In this sense, the two parameters automatically fine-tuned were w_{df}^{fixed} and w_{reg}^{fixed}, since these two parameters correspond to data fidelity and regularization parameters, for which the proposed framework has been formulated. Li *et al*. minimize an energy functional inspired by the GAC energy functional [10], which is defined as

$$E(\phi) = w_{reg}^{fixed} \int_{\Omega} p(|\nabla \phi|dx + a^{fixed} \int_{\Omega} g\delta_{\varepsilon}(\phi)|\nabla \phi|dx + w_{df}^{fixed} \int_{\Omega} gH_{\varepsilon}(-\phi)dx \tag{12}$$

where ϕ is the level set function, p a potential function p:$[0, \infty) \rightarrow \Re$, g an edge-indicator function, δ the Dirac function, H the Heaviside function, w_{reg}^{fixed} the fixed regularization parameter, a^{fixed} a fixed parameter that weights the second energy term which can be expressed as a line integral of the GAC model, and w_{df}^{fixed} the fixed data fidelity parameter. The level set evolution is determined as follows:

$$\frac{\partial \phi}{\partial t} = w_{reg}^{fixed} \cdot div\left(d_p \frac{\nabla \phi}{|\nabla \phi|}\right) + a^{fixed}\delta_{\varepsilon}(\phi) \cdot div\left(g\frac{\nabla \phi}{|\nabla \phi|}\right) + w_{df}^{fixed} g\delta_{\varepsilon}(\phi). \tag{13}$$

For the empirical case, the optimal fixed parameters are set according to the original paper [17]. For the proposed framework, the optimal fixed value of a^{fixed} is maintained, whereas the regularization and data fidelity parameters are automatically calculated according to (6). The value of a^{fixed} remained empirically fixed and its adjustment is beyond the scope of this paper. However, the presence of the extra term in this model did not prevent the proposed framework to automatically adjust w_{reg}^{fixed} and w_{df}^{fixed}.

In a similar fashion, the segmentation performance of both empirical and automated versions of the model of Li *et al*. [17] is evaluated on test images obtained by the author's homepage [52]. Fig. 15(a) and (b) illustrates a test image and the initial level-set function, respectively, whereas the images below present contours obtained in three different iterations, as well as the final level-set functions. The latter exhibit the shape of a signed distance function in the vicinity of the zero level-set and a flat shape outside this vicinity. Red and green colors correspond to empirical and automated parameterization, respectively. It should be pointed out that the level-set evolution is applied without reinitialization and is guided also by edge-based forces. It is evident that the segmentation results of the empirical and automated versions are comparable.

Fig. 16 depicts TC results of both empirical and automated versions for the early stages of contour evolution presented in Fig. 15. In the automated version, TC reaches slightly higher values from early iterations. However, one should take into account that with empirical parameterization it is always possible to set "optimal" parameters after laborious, time-consuming experimentation. Our framework is capable of obtaining comparable results in an automated fashion.

E. Rudin–Osher–Fatima (ROF) Model [50]

The proposed framework is also integrated into the ROF model for edge-preserving image restoration, so as to test its effectiveness on other inverse minimization problems (TV minimization). The aim of the ROF model is to remove noise from a corrupted image without blurring the target edges. Let $f = K * I + n$ denote the image plagued by noise, where K, n are the convolution kernel and additive noise, respectively. The "clean" image is recovered by minimizing the following energy:

$$E(I) = \int_{\Omega} |\nabla I| + w_{df}^{fixed} \int_{\Omega} (f - I)^2 dx. \tag{14}$$

For the empirical case, the optimal fixed parameter is set according to the original paper [50]. For the proposed framework, the data fidelity parameter is automatically calculated according to (6). Fig. 17 illustrates: (a) the original image plagued by noise, (b) the recovered image of the ROF model utilizing empirical parameterization, and (c) the recovered image of the ROF model utilizing automated parameterization. In [50], image restoration is visually assessed. Following this, it can be observed that, the automated version maintains the quality of image restoration, originally obtained with empirical parameters.

F. Nikolova et al. Model [51]

The Nikolova *et al*. model solve the following nonconvex nonsmooth minimization problem for image restoration and reconstruction:

$$J(I, u) = ||HI - g||_2^2 + \beta\Psi(I) + \beta\alpha TV(u) + w_{df}^{fixed}||I - u||_2^2 \tag{15}$$

This article has been accepted for inclusion in a future issue of this journal. Content is final as presented, with the exception of pagination.

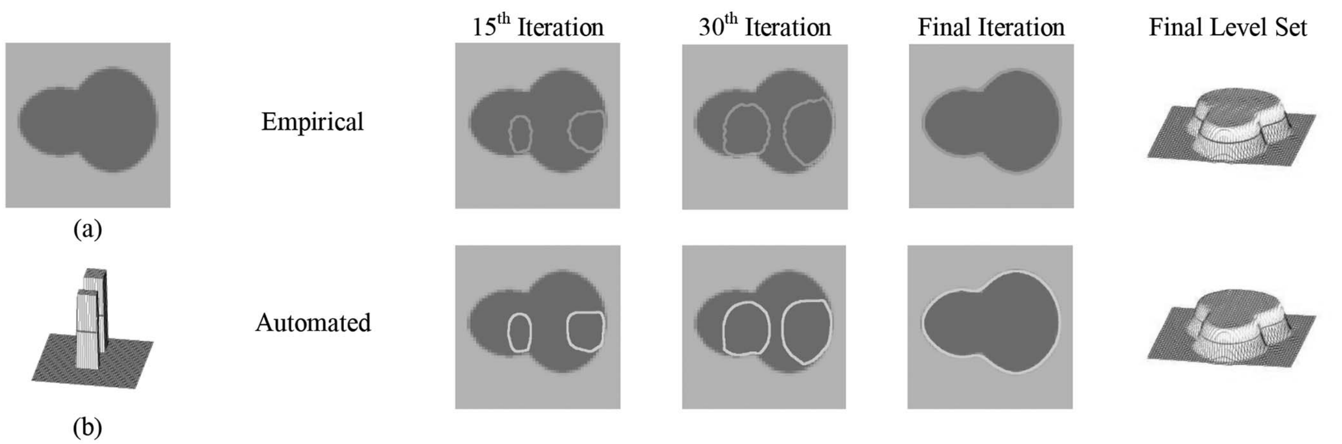

Fig. 15. Evolution of segmentation for the model of Li *et al*. Red and green contour corresponds to empirical ($w_{reg}^{fixed} = 0.2$, $w_{df}^{fixed} = 5$) and automated parameterization, respectively. (a) Original test image. (b) Initial level-set function. Size 56×56.

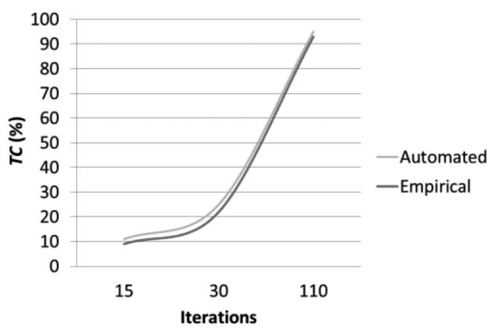

Fig. 16. TC for the early stages of evolution of automated versus empirical model presented in Fig. 15.

where H is a $q \times p$ matrix representing optical blurring, $\Psi(\mathrm{I}) = \sum_{i \in I} \psi_{\varepsilon}(||D_i I||_2$, where ψ is a smooth and concave function and D_i discrete gradients, g the image plagued by noise, $u \in \Re$ an auxiliary variable used to transfer the nonsmooth TV term from image I and β, α the restoration parameters, where β is a regularization parameter and α a positive parameter. In the case of empirical fine-tuning, the fixed parameter w_{df}^{fixed} is set according to the original paper [51]. In the case of the proposed framework, the data fidelity parameter is automatically calculated according to (6). Fig. 18 illustrates: (a) the original image, (b) the observed image, (c) the result of empirically parameterized restoration, and (d) the result of restoration parameterized by means of (6). It is once more evident that, the proposed framework maintains the quality of image restoration compared to the one obtained by empirical parameterization. In more quantitative terms, the point-to-signal-noise-ratio (PSNR) obtained by empirical and automated parameterization is 18.65 and 18.59 dB, respectively.

Considering both the ROF model and the Nikolova *et al*. model, it should be highlighted that, even though the proposed framework has been designed for segmentation models, it can also be effectively embedded in other energy minimization models, with similar formulation, as is the case of these two restoration models.

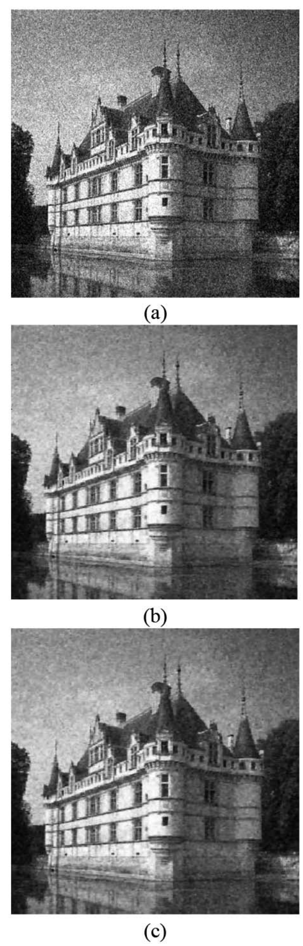

Fig. 17. (a) Original image plagued by noise, the recovered image of the ROF model utilizing. (b) Empirical parameterization ($w_{df}^{fixed} = 12$). (c) Automated parameterization. Size 320×320.

G. Additional Experiments on Various Datasets

The proposed framework is also tested on 20 grayscale images obtained by the ALOI database [60], 20 coronal scans obtained by the LIDC-IDRI [61], 20 thyroid ultrasound

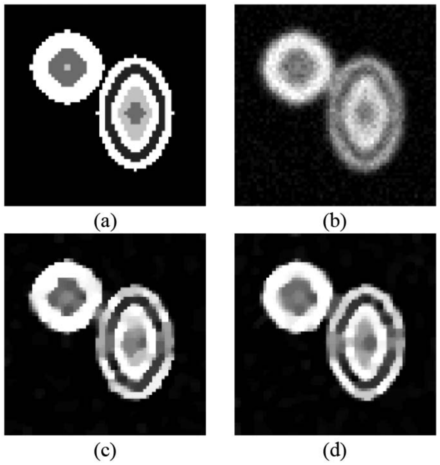

Fig. 18. (a) Original image plagued by noise. (b) Observed image. (c) Restored image utilizing empirical parameterization ($w_{df}^{fixed} = 0.05$). (d) Restored image utilizing automated parameterization. Size 64 × 64.

images containing hypoechoic nodules provided by the radiology department of Euromedica S.A., Greece and 20 images obtained by the LTG-IDB [62] in order to enable evaluation on large benchmark datasets.

Fig. 19 illustrates segmentation results on sample images obtained by the ALOI database for both empirical and automated parameterization. The first and second columns illustrate test images and their ground truth, respectively. The third column provides the iteration number, for which the automated version converges. The fourth and fifth columns illustrate segmentation results of the empirical and automated case for that iteration, respectively. The sixth and seventh columns illustrate the iteration number for which the empirical version converges and the segmentation results for that iteration, respectively. All test images were recorded with varying viewing and illumination angles, resulting in challenging shades. Several images of ALOI database, including the illustrated *Teapot*, *Bear*, *Basket*, and *Wire*, contain intensity-based information whereas some also contain textured regions, as is the case with *Basket* and *Wire*. It is evident that after convergence, the segmentation results of both empirical and automated versions are comparable. However, in the empirical case, the contour is delayed on erroneous local intensity minima associated with shades and thus requires approximately 10–20 times more iterations in order to converge. On the contrary, in the automated case, forces which guide contour evolution are appropriately amplified in nontarget, high-entropy edges, accelerating convergence. The automated case achieves an average TC value of 96.9 ± 1.6%, which is comparable to the TC value obtained by the empirical case. However, the empirical case achieves a TC value of 58.4 ± 14.3% in the same iteration that the automated version has converged, with regards to all ALOI images tested.

Fig. 20 illustrates: (a)–(c) sample coronal computed-tomography scans of lung parenchyma, (a_1)–(c_1) ground truth images, (a_2)–(c_2) segmentation results of the empirical version, (a_3)–(c_3) segmentation results of the automated version. The aim of segmentation on this database (LIDC-IDRI) is to separate the lung parenchyma from the surrounding anatomy, which is typically impeded by airways or other "airway-like" structures in the right and left lung. The segmentation result is used for the computation of emphysema measures. Such images contain an inhomogeneous background and multiple features, such as the trachea and thoracic spine (pale areas), as well as the left and right lung (dark areas). It is notable that both versions achieve comparable segmentation results. The automated version achieves an average TC value of 83.8 ± 1.3%, over all computed-tomography scans of the database, which is comparable to the TC value of 82.5 ± 1.8% obtained by the empirical version.

Fig. 21 illustrates: (a)–(c) sample thyroid ultrasound images containing hypoechoic nodules, (a_1)–(c_1) ground truth images, (a_2)–(c_2) segmentation results of the empirical version, (a_3)–(c_3) segmentation results of the automated version. Hypoechoic nodules may be associated with medium or high risk for malignancy, depending on the irregularity of their boundary. These images are very challenging with respect to segmentation, since they are plagued by speckle noise and artifacts. Moreover, thyroid nodules are characterized by blurred and irregular boundaries. It can be observed that the segmentation result of the automated version is comparable to the one obtained by the empirical version. The automated version achieves an average TC value of 83.7 ± 0.8%, over all thyroid ultrasound images of the database, which is comparable to the TC value of 82.8 ± 1.2% obtained by the empirical version.

Fig. 22 illustrates: (a)–(c) labial teeth and gingiva photographic images, (a_1)–(c_1) ground truth images, (a_2)–(c_2) segmentation results of the empirical version, (a_3)–(c_3) segmentation results of the automated version. The scope of this database (LTG-IDB) is the task of teeth/nonteeth segmentation. Such images are characterized by intensity variations from saturated to faint areas, over an inhomogeneous background (gingiva). It can be observed that the segmentation results obtained by the automated version approximate the corresponding ground truth images. The automated version achieves an average TC value of 84.2 ± 1.8%, over all images of the database, which is comparable to the TC value of 82.9 ± 1.6% obtained by the empirical version.

IV. Conclusion and Future Directions

This paper introduces a novel framework for automated regularization and data fidelity parameterization of region-based ACs, which is motivated by the observation that the weighting factors of regularization and data fidelity terms and the eigenvalues of structure tensors are associated with the same orthogonal directions. The proposed framework is unsupervised and does not require technical skills from the domain user. In addition, it is applicable to several image modalities and does not require prior knowledge on the target regions. Moreover, it avoids iterations dedicated to erroneous local minima, resulting in convergence rate comparable to or higher than the one obtained with empirical parameterization.

The proposed framework has been experimentally evaluated on various datasets of natural, textured, and biomedical images

This article has been accepted for inclusion in a future issue of this journal. Content is final as presented, with the exception of pagination.

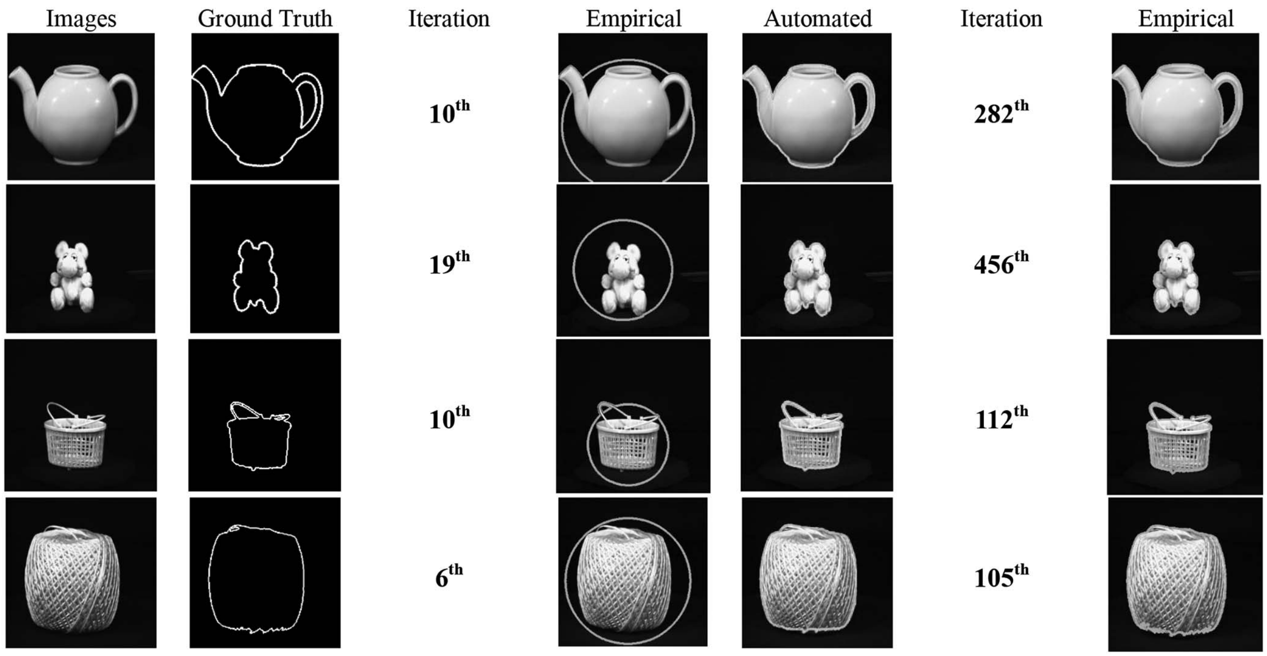

Fig. 19. Segmentation results of the proposed framework. The first and second columns illustrate test images obtained by ALOI database [60] and their ground truth images, respectively. The third column shows the final iteration of contour convergence in the automated case. The fourth and fifth column illustrates segmentation results of the empirical ($w_{reg}^{fixed} = 0.006 \cdot 255^2$, $w_{df}^{fixed} = 1$) and automated case for that iteration, respectively. The sixth and seventh column illustrates the final iteration of contour convergence in the empirical case as well as the segmentation results for that iteration, respectively. Size 320×320.

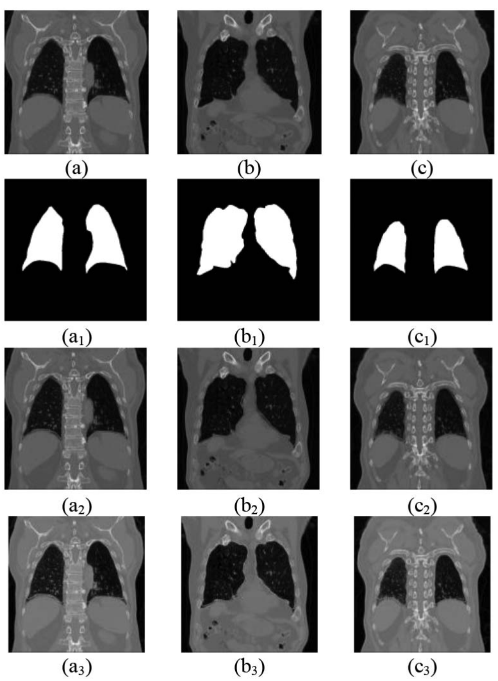

Fig. 20. (a)–(c) Coronal computed-tomography scans of lung parenchyma. (a_1)–(c_1) Ground truth images. (a_2)–(c_2) Segmentation results of the empirical version ($w_{reg}^{fixed} = 0.006 \cdot 255^2$, $w_{df}^{fixed} = 1$). (a_3)–(c_3) Segmentation results of the automated version. Size 320×320.

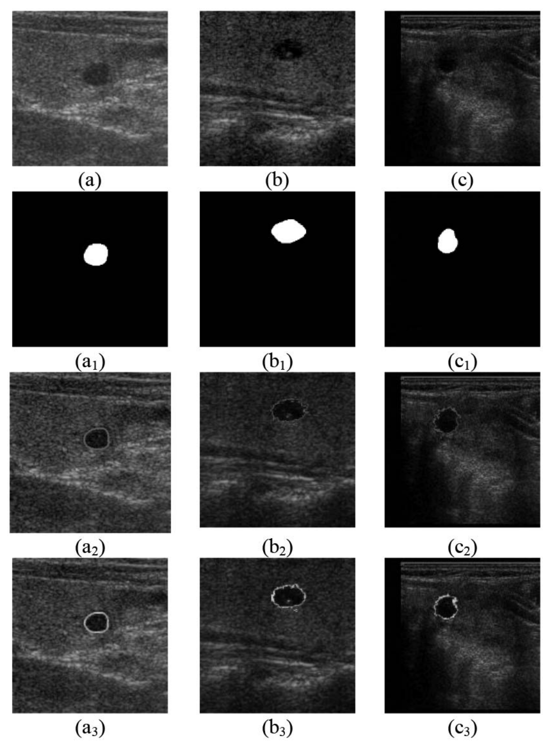

Fig. 21. (a)–(c) Thyroid ultrasound images containing nodules. (a_1)–(c_1) Ground truth images. (a_2)–(c_2) segmentation results of the empirical version ($w_{reg}^{fixed} = 0.006 \cdot 255^2$, $w_{df}^{fixed} = 1$). (a_3)–(c_3) Segmentation results of the automated version. Size 256×256.

by comparing the segmentation performance obtained by empirical versus automated parameterization of four state-of-the-art region-based AC variations and two image restoration models. The experimental results show that it is capable of maintaining a segmentation quality comparable to the one obtained with empirical parameterization, yet in an automated fashion. Future directions of this paper include investigation

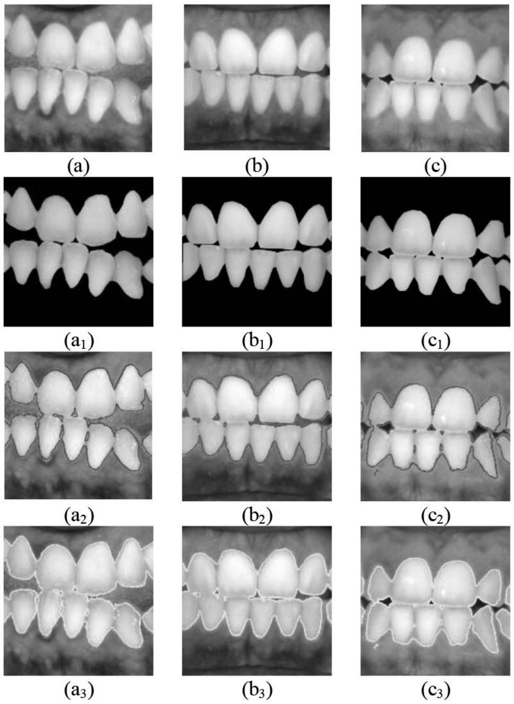

Fig. 22. (a)–(c) Labial teeth and gingiva photographic images. (a_1)–(c_1) Ground truth images. (a_2)–(c_2) Segmentation results of the empirical version ($w_{reg}^{fixed} = 0.006 \cdot 255^2$, $w_{df}^{fixed} = 1$). (a_3)–(c_3) Segmentation results of the automated version. Size 320×320.

of the potential of alternative instances of the proposed framework on several biomedical application domains.

Acknowledgment

The authors would like to thank Prof. R. Deriche for his fruitful comments during his visit to the Department of Informatics and Telecommunications of the National and Kapodistrian University of Athens. They would also like to thank the Biomedical Research Foundation of the Academy of Athens for the provision of real 2D-GE images, and Dr. N. Dimitropoulos, MD Radiologist, EUROMEDICA S.A., Greece, for providing the thyroid ultrasound images. They are grateful to the reviewers for their constructive comments and suggestions.

References

[1] Y. Rathi, N. Vaswani, A. Tannenbaum, and A. Yezzi, "Tracking deformable objects using particle filtering for geometric active contours," *IEEE Trans. Pattern Anal. Mach. Intell.*, vol. 29, no. 8, pp. 1470–1475, Aug. 2007.

[2] G. Sundaramoorthi, A. Yezzi, and A. Mennucci, "Coarse-to-fine segmentation and tracking using Sobolev active contours," *IEEE Trans. Pattern Anal. Mach. Intell.*, vol. 30, no. 5, pp. 851–864, May 2008.

[3] A. Mishra, P. W. Fieguth, and D. A. Clausi, "From active contours to active surfaces," in *Proc. IEEE CVPR*, Providence, RI, USA, 2011, pp. 2121–2128.

[4] V. Appia and A. Yezzi, "Active geodesics: Region-based active contour segmentation with a global edge-based constraint," in *Proc. IEEE ICCV*, Barcelona, Spain, 2011, pp. 1975–1980.

[5] H. Xiao, Y. Li, J. Du, and A. Mosig, "Ct3d: Tracking microglia motility in 3D using a novel cosegmentation approach," *Bioinformatics*, vol. 28, no. 4, pp. 564–571, 2011.

[6] M. Kass, A. Witkin, and D. Terzopoulos, "Snakes: Active contour models," *Int. J. Comput. Vis.*, vol. 1, no. 4, pp. 321–331, 1988.

[7] V. Caselles, R. Kimmel, and G. Sapiro, "Geodesic active contours," in *Proc. IEEE ICCV*, Cambridge, MA, USA, 1995, pp. 694–699.

[8] S. Kichenassamy, A. Kumar, P. Olver, A. Tannenbaum, and A. Yezzi, "Gradient flows and geometric active contour models," in *Proc. IEEE ICCV*, Cambridge, MA, USA, 1995, pp. 810–815.

[9] R. Malladi, J. A. Sethian, and B. C. Vemuri, "Shape modeling with front propagation: A level set approach," *IEEE Trans. Pattern Anal. Mach. Intell.*, vol. 17, no. 2, pp. 158–175, Feb. 1995.

[10] N. Paragios and R. Deriche, "Geodesic active contours and level sets for the detection and tracking of moving objects," *IEEE Trans. Pattern Anal. Mach. Intell.*, vol. 22, no. 3, pp. 266–280, Mar. 2000.

[11] S. Osher and J. Sethian, "Fronts propagating with curvature-dependent speed: Algorithms based on the Hamilton–Jacobi formulation," *J. Comput. Phys.*, vol. 79, no. 1, pp. 12–49, 1988.

[12] M. Leventon, W. Grimson, and O. Faugeras, "Statistical shape influence in geodesic active contours," in *Proc. IEEE Conf. CVPR*, vol. 1. Hilton Head Island, SC, USA, 2000, pp. 316–323.

[13] J. Daugman, "New methods in iris recognition," *IEEE Trans. Syst., Man, Cybern. B, Cybern.*, vol. 37, no. 5, pp. 1167–1175, Oct. 2007.

[14] N. Paragios, O. Mellina-Gottardo, and V. Ramesh, "Gradient vector flow fast geometric active contours," *IEEE Trans. Pattern Anal. Mach. Intell.*, vol. 26, no. 3, pp. 402–407, Mar. 2004.

[15] C. Li, C. Xu, C. Gui, and M. D. Fox, "Level set evolution without reinitialization: A new variational formulation," in *Proc. IEEE Conf. CVPR*, vol. 1. 2005, pp. 430–436.

[16] X. Xie and M. Mirmehdi, "MAC: Magnetostatic active contour model," *IEEE Trans. Pattern Anal. Mach. Intell.*, vol. 30, no. 4, pp. 632–646, Apr. 2008.

[17] C. Li, C. Xu, C. Gui, and M. D. Fox, "Distance regularized level set evolution and its application to image segmentation," *IEEE Trans. Image Process.*, vol. 19, no. 12, pp. 3243–3254, Dec. 2010.

[18] D. Mumford and J. Shah, "Boundary detection by minimizing functionals," in *Proc. IEEE Conf. CVPR*, 1985, pp. 22–26.

[19] T. F. Chan and L. A. Vese, "Active contours without edges," *IEEE Trans. Image Process.*, vol. 10, no. 2, pp. 266–277, Feb. 2001.

[20] A. Tsai, A. Yezzi, and A. S. Willsky, "Curve evolution implementation of the Mumford–Shah functional for image segmentation, denoising, interpolation and magnification," *IEEE Trans. Image Process.*, vol. 10, no. 8, pp. 1169–1186, Aug. 2001.

[21] L. A. Vese and T. F. Chan, "A multiphase level set framework for image segmentation using the Mumford and Shah model," *Int. J. Comput. Vis.*, vol. 50, no. 3, pp. 271–293, 2002.

[22] D. Freedman and T. Zhang, "Active contours for tracking distributions," *IEEE Trans. Image Process.*, vol. 13, no. 4, pp. 518–526, Apr. 2004.

[23] P. Li, "Tensor-SIFT based earth mover's distance for contour tracking," *J. Math. Imaging Vis.,* vol. 46, no. 1, pp. 44–65, 2013.

[24] S. Jehan-Besson, M. Barlaud, G. Aubert, and O. Faugeras, "Shape gradients for histogram segmentation using active contours," in *Proc. IEEE ICCV*, Nice, France, 2003, pp. 408–415.

[25] T. Brox and D. Cremers, "On local region models and a statistical interpretation of the piecewise smooth Mumford-Shah functional," *Int. J. Comput. Vis.*, vol. 84, no. 2, pp. 184–193, Aug. 2009.

[26] X. Bresson, S. Esedoglu, P. Vandergheynst, J. Thiran, and S. Osher, "Fast global minimization of the active contour/snake model," *J. Math. Imaging Vis.*, vol. 28, no. 2, pp. 151–167, 2007.

[27] E. Strekalovskiy, A. Chambolle, and D. Cremers, "A convex representation for the vectorial Mumford-Shah functional," in *Proc. IEEE Conf. CVPR*, Providence, RI, USA, 2012.

[28] N. Paragios and R. Deriche, "Geodesic active regions and level set methods for supervised texture segmentation," *Int. J. Comput. Vis.*, vol. 46, no. 3, pp. 223–247, 2002.

[29] C. Li, C. Kao, J. Gore, and Z. Ding, "Implicit active contours driven by local binary fitting energy," in *Proc. IEEE Conf. CVPR*, Minneapolis, MN, USA, 2007, pp. 1–7.

[30] S. Lankton and A. Tannenbaum, "Localizing region-based active contours," *IEEE Trans. Image Process.*, vol. 17, no. 11, pp. 2029–2039, Nov. 2008.

[31] R. S. T. Lee and J. N. K. Lin, "An elastic contour matching model for tropical cyclone pattern recognition," *IEEE Trans. Syst., Man, Cybern. B, Cybern.*, vol. 31, no. 3, pp. 413–417, Jun. 2001.

[32] L. Wang, C. Li, Q. Sun, D. Xia, and C. Kao, "Active contours driven by local and global intensity fitting energy with application to brain MR image segmentation," *Comput. Med. Imaging Graph.*, vol. 33, no. 7, pp. 520–531, 2009.

[33] B. Wu and Y. Yang, "Local- and global-statistics-based active contour model for image segmentation," *Math. Probl. Eng.*, vol. 64, Article 791958, Jan. 2012.

[34] C. Pluempitiwiriyawej, J. M. F. Moura, Y. J. L. Wu, and C. Ho, "STACS: New active contour scheme for cardiac MR image segmentation," *IEEE Trans. Med. Imag.*, vol. 24, no. 5, pp. 593–603, May 2005.

[35] A. Tsai *et al.*, "A shape-based approach to the segmentation of medical imagery using level sets," *IEEE Trans. Med. Imag.*, vol. 22, no. 2, pp. 137–154, Feb. 2003.

[36] I. Kokkinos, G. Evangelopoulos, and P. Maragos, "Texture analysis and segmentation using modulation features, generative models and weighted curve evolution," *IEEE Trans. Pattern Anal. Mach. Intell.*, vol. 31, no. 1, pp. 142–157, Jan. 2009.

[37] M. Keuper *et al.*, "3D deformable surfaces with locally self-adjusting parameters—A robust method to determine cell nucleus shapes," in *Proc. IEEE ICPR*, Washington, DC, USA, 2010, pp. 2254–2257.

[38] X. Liu, Y. M. Cheung, M. Li, and H. Liu, "A lip extraction method using localized active contour model with automatic parameter selection," in *Proc. IEEE ICPR*, Istanbul, Turkey, 2010, pp. 4332–4335.

[39] D. Iakovidis, M. Savelonas, S. Karkanis, and D. Maroulis, "A genetically optimized level set approach to segmentation of thyroid ultrasound images," *Appl. Intell.*, vol. 27, no. 3, pp. 193–203, Dec. 2007.

[40] C. Y. Hsu, C. Y. Liu, and C. M. Chen, "Automatic segmentation of liver PET images," *Comput. Med. Imaging Graph.*, vol. 32, no. 7, pp. 601–610, 2008.

[41] M. Allili and D. Ziou, "An approach for dynamic combination of region and boundary information in segmentation," in *Proc. IEEE ICPR*, Tampa, FL, USA, 2008, pp. 1–4.

[42] P. A. Yushkevich *et al.*, "User-guided level set segmentation of anatomical structures with ITK–SNAP," in *Proc. Insight J., Special Issue ISC/NA-MIC/MICCAI Workshop Open-Source Software*, 2005.

[43] E. A. Mylona, M. A. Savelonas, and D. Maroulis, "Entropy-based spatially-varying adjustment of active contour parameters," in *Proc. IEEE ICIP*, Orlando, FL, USA, 2012, pp. 2565–2568.

[44] E. A. Mylona, M. A. Savelonas, D. Maroulis, and A. N. Skodras, "Autopilot spatially-adaptive active contour parameterization for medical image segmentation," in *Proc. IEEE Int. Symp. CBMS*, Porto, Portugal, 2013.

[45] D. Tschumperlé and R. Deriche, "Vector-valued image regularization with PDEs: A common framework for different applications," *IEEE Trans. Pattern Anal. Mach. Intell.*, vol. 27, no. 4, pp. 506–517, Apr. 2005.

[46] J. Weickert and H. Scharr, "A scheme for coherence-enhancing diffusion filtering with optimized rotation invariance," *J. Visual Commun. Image Rep.*, vol. 13, no. 1–2, pp. 103–118, Mar. 2002.

[47] M. N. Do and M. Vetterli, "The contourlet transform: An efficient directional multiresolution image representation," *IEEE Trans. Image Process.*, vol. 14, no. 12, pp. 2091–2106, Dec. 2005.

[48] M. Vetterli, "Multidimensional subband coding: Some theory and algorithms," *IEEE Trans. Signal Process.*, vol. 6, no. 2, pp. 97–112, Apr. 1984.

[49] M. A. Savelonas, E. A. Mylona, and D. Maroulis, "Unsupervised 2D gel electrophoresis image segmentation based on active contours," *Pattern Recognit.*, vol. 45, no. 2, pp. 720–731, Feb. 2012.

[50] L. I. Rudin, S. Osher, and E. Fatemi, "Nonlinear total variation based noise removal algorithms," *Physica D*, vol. 60, no. 1–4, pp. 259–268, 1992.

[51] M. Nikolova, M. K. Ng, and C. P. Tam, "Fast nonconvex nonsmooth minimization methods for image restoration and reconstruction," *IEEE Trans. Med. Imag.*, vol. 19, no. 12, pp. 3073–3088, Dec. 2010.

[52] C. Li. (2011). *University of Connecticut* [Online]. Available: http://www.engr.uconn.edu/˜cmli/

[53] X. Bresson. (2010). *City University of Hong Kong* [Online]. Available: http://www.cs.cityu.edu.hk/˜xbresson/

[54] [Online]. Available: http://www.mathworks.com/matlabcentral/fileexchange/22410-rof-denoising-algorithm

[55] [Online]. Available: http://www.math.hkbu.edu.hk/˜mng/

[56] D. D.-Y. Po and M. N. Do, "Directional multiscale modeling of images using the contourlet transform," *IEEE Trans. Image Process.*, vol. 15, no. 6, pp. 1610–1620, Jun. 2006.

[57] P. Arbelaez, M. Maire, C. Fowlkes, and J. Malik, "Contour detection and hierarchical image segmentation," *IEEE Trans. Pattern Anal. Mach. Intell.*, vol. 33, no. 5, pp. 898–916, May 2011.

[58] A. K. Mishra, P. W. Fieguth, and D. A. Clausi, "Decoupled active contour (DAC) for boundary detection," *IEEE Trans. Pattern Anal. Mach. Intell.*, vol. 33, no. 2, pp. 310–324, Feb. 2011.

[59] L. Bertelli, B. Sumengen, B. S. Manjunath, and F. Gibou, "A variational framework for multiregion pairwise-similarity-based image segmentation," *IEEE Trans. Pattern Anal. Mach. Intell.*, vol. 30, no. 8, pp. 1400–1414, Mar. 2008.

[60] J. M. Geusebroek, G. J. Burghouts, and A. W. M. Smeulders, "The Amsterdam library of object images," *Int. J. Comput. Vis.*, vol. 61, no. 1, pp. 103–112, 2005.

[61] [Online]. Available: http://www.cancerimagingarchive.net

[62] T. Eckhard, E. M. Valero, and J. L. Nieves, "Labial teeth and gingiva color image segmentation for gingival health-state assessment," in *Proc. Eur. Conf. CGIV*, 2012, pp. 102–107.

[63] W. R. Crum, O. Camara, and D. L. G. Hill, "Generalized overlap measures for evaluation and validation in medical image analysis," *IEEE Trans. Med. Imag.*, vol. 25, no. 11, pp. 1451–1461, Nov. 2006.

[64] B. Mory and R. Ardon, "Fuzzy region competition: A convex two-phase segmentation framework," in *Scale Space and Variational Methods in Computer Vision*, vol. 4485. Berlin, Germany: Springer, 2007, pp. 214–226.

Eleftheria A. Mylona received the B.Sc. degree in applied mathematical and physical sciences from the National Technical University of Athens, Athens, Greece, the M.Sc. degree in physics from the University of Edinburgh, Scotland, U.K., and the Ph.D. degree in image analysis from the University of Athens, Athens, Greece, in 2006, 2007, and 2014, respectively.

Currently, she is affiliated with the Institute for Astronomy, Astrophysics, Space Applications and Remote Sensing, National Observatory of Athens, Athens, Greece. She has co-authored 16 research articles on biomedical image analysis. Her current research interests include pattern recognition and image analysis.

Ms. Mylona received a scholarship co-financed by the European Union and Greek National funds during the Ph.D. research.

Michalis A. Savelonas (M'08) received the B.Sc. degree in physics, the M.Sc. (Hons.) degree in cybernetics, and the Ph.D. (Hons.) degree in the area of image analysis from the University of Athens, Athens, Greece, in 1998, 2001, and 2008, respectively.

Among positions in various academic institutions, including University of Athens, University of Houston, TX, USA, Hellenic Air Force Academy and Technological and Educational Institute of Lamia, he is currently a Research Fellow with Athena Research and Innovation Center, Xanthi, Greece. He has co-authored over 50 research articles and book chapters, and has been actively involved in several EU, US and Greek Research and Development projects. From 2002 to 2004, he was with software industry for the development of real-time systems. His current research interests include image analysis, segmentation, pattern recognition, bioinformatics, and watermarking.

Dr. Savelonas received a scholarship from the Greek General Secretariat of Research and Technology and the European Social Fund for the Ph.D. research. He is a Reviewer in prestigious international journals including IEEE TRANSACTIONS ON IMAGE PROCESSING and PATTERN RECOGNITION.

Dimitris Maroulis (M'02) received the B.Sc. degree in physics, the M.Sc. degree in Radioelectricity (Hons.), the M.Sc. degree in Cybernetics, and the Ph.D. (Hons.) degree in computer science, all from the University of Athens, Athens, Greece.

He served as a Research Fellow for 3 years at the Space Research Department of Meudon Observatory, Paris, France, and afterwards, he collaborated for over 10 years with the same Department. He was with the Hellenic Telecommunications Organization (PTT, Department of Statistics) for 2 years. He served as Lecturer, Assistant and Associate Professor at the Departments of Physics and Informatics of the University of Athens. Currently, he is a Professor at the same University and leader of the Real-Time Systems and Image Analysis Lab (RTS-image). He has over 20 years of experience in the areas of data acquisition and real-time systems, and over 15 years of experience in the area of image/signal analysis and processing. He has also been collaborating with many Greek and European hospitals and health centers for over 15 years in the field of biomedical informatics. He has been actively involved in over 12 European and National Research and Development projects and has been the Project Leader of five of them, all in the areas of image/signal analysis and real-time systems. He has published over 150 research papers and book chapters, and currently, there are over 1400 citations that refer to his published work. He has made peer reviews for over 12 international journals, as well as for an equal number of international conferences. His current research interests include data acquisition and real-time systems, pattern recognition, image analysis, with applications on biomedical systems, and bioinformatics.